data were used to determine the photoanation quantum yields relative to $[(bpy)_3Ru]^{2+}$.

Acknowledgment. R.H.S. thanks the Louisiana Educational Quality Support Fund, administered by the Louisiana State Board of Regents, for support of this work. We acknowledge financial support from EOLAS, the Irish Science and Technology Agency. We also thank Johnson Matthey for a generous load of ruthenium trichloride.

Appendix

Ireland and Wyatt[28] and others have stated the general solution for luminescence decay of protonated and deprotonated species in equilibrium (Scheme I). The solution for particular cases requires knowledge of five constants: the ground-state acid dissociation constant (K_{ag}), the decay rate constants of the protonated (k_{nrH}) and deprotonated (k_{nr}) complexes, and the rate constants for protonation (k_H) and deprotonation (k_{-H}) of the excited complex. By assuming both the protonated (HPTN) and deprotonated (PTN) complexes have the same molar absorptivity at the excitation wavelength (λ = 337 nm),[35] the fractions, f, of PTN and HPTN in solution immediately following excitation at any given pH can be determined from K_{ag}:

$$[PTN]_T = [HPTN]_0 + [PTN]_0$$

$$f^0_{HPTN} = [HPTN]_0/[PTN]_T = [H^+]/(K_{ag} + [H^+])$$

$$f^0_{PTN} = [PTN]_0/[PTN]_T = 1 - [HPTN]_0$$

The concentration of excited PTN and HPTN at any time following excitation can be written from the general expression of Ireland and Wyatt (see Scheme I):[28]

$$\frac{[PTN]_t}{[PTN]_T} = \frac{1}{2\lambda}\{[(\lambda - k_p + k_d)f^0_{PTN} - 2k_{-H}f^0_{HPTN}]\exp(-\alpha t) + [(\lambda + k_p - k_d)f^0_{PTN} + 2k_{-H}f^0_{HPTN}]\exp(-\beta t)\} \quad (A1)$$

$$\frac{[HPTN]_t}{[PTN]_T} = \frac{1}{2\lambda}\{[(\lambda + k_p - k_d)f^0_{HPTN} - 2k_H[H^+]f^0_{PTN}] \times \exp(-\alpha t) + [(\lambda - k_p + k_d)f^0_{HPTN} + 2k_H[H^+]f^0_{PTN}]\exp(-\beta t)\} \quad (A2)$$

$$\lambda = \sqrt{(k_p - k_d)^2 + 4k_{-H}k_H[H^+]}$$

$$\alpha = (k_p + k_d + \lambda)/2$$

$$\beta = (k_p + k_d - \lambda)/2$$

$$k_p = k_{nrH} + k_{-H} \qquad k_d = k_{nr} + k_H[H^+]$$

Since decay of the protonated complex is very fast ($k_{nrH} \sim 2$-5×10^8 s^{-1}), it is assumed that the predominant emitting species in solution at times >10 ns is the deprotonated complex. Data were fit to eq A1 by using experimental values of K_{ag}, k_{nrH}, and k_{nr}, assuming a value of K_{ae}, and having a single variable parameter, k_H ($k_{-H} = K_{ae}k_H$). Figure 7 illustrates results obtained using this fitting procedure.

Time-Resolved Charge-Transfer Spectroscopy of Aromatic EDA Complexes with Nitrosonium. Inner-Sphere Mechanism for Electron Transfer in the Isoergonic Region

T. M. Bockman, Z. J. Karpinski, S. Sankararaman, and J. K. Kochi*

Contribution from the Chemistry Department, University of Houston, Houston, Texas 77204-5641. *Received December 17, 1990. Revised Manuscript Received October 29, 1991*

Abstract: Photoinduced electron transfer in various 1:1 aromatic EDA complexes with nitrosonium by the direct laser-pulse (20-ps and 10-ns fwhm) excitation of the charge-transfer bands leads to the spontaneous generation of the redox pair $Ar^{\bullet+}$ and NO. Temporal relaxation by back electron transfer to regenerate the EDA complex $[Ar,NO^+]$ is measured by following the spectral decay of $Ar^{\bullet+}$ with the aid of time-resolved spectroscopy over the two separate time domains I and II. *Picosecond kinetics* (k_1) are associated with the first-order collapse of the geminate ion radical $[Ar^{\bullet+},NO]$ by inner-sphere electron transfer back to the EDA complex—the relatively slow rates with $k_1 \sim 10^8$ s^{-1} arising from driving forces that approach the isoergonic region, coupled with the rather high reorganization energy of nitric oxide. These allow effective competition from diffusive separation (k_s) to form $Ar^{\bullet+}$ and NO as kinetically separate entities. *Microsecond kinetics* (k_{II}) are thus associated with the second-order (back) electron transfer from the freely diffusing $Ar^{\bullet+}$ and NO. However, the comparison of the second-order rate constants calculated from Marcus theory shows that outer-sphere electron transfer is too slow to account for the experimental values of k_{II}. The second-order process is unambiguously identified (by the use of the thermochemical cycle in Scheme IV) as the alternative, more circuitous inner-sphere pathway involving the (re)association (k_a) of $Ar^{\bullet+}$ and NO to afford the cation radical pair $[Ar^{\bullet+},NO]$ followed by its collapse to the EDA complex. The general implications of inner-sphere complexes as reactive intermediates in electron transfer mechanisms in the isoergonic and endergonic regions are presented.

Introduction

The nitrosonium ion NO^+ is an unusually versatile species—a simple diatomic cation that is coordinatively unsaturated, easily formed, and uncommonly persistent in solution.[1] Being isoelectronic with carbon monoxide, NO^+ is an excellent ligand;[2] but it has also been used as an active electrophile[3] as well as an effective oxidant[4] in electron-transfer processes due to its rather

(1) Cotton, F. A.; Wilkinson, G. *Advanced Inorganic Chemistry*; 5th ed.; Wiley: New York, 1988; p 321 ff.

(2) (a) McCleverty, J. A. *Chem. Rev.* **1979**, *79*, 53. (b) Feltham, R. D.; Enemark, J. H. In *Topics in Inorganic and Organometallic Stereochemistry*; Geoffroy, G., Ed.; Wiley: New York, 1981. (c) Pandey, K. K. *Coord. Chem. Rev.* **1983**, *51*, 69. (d) Hawkins, T. W.; Hall, M. B. *Inorg. Chem.* **1980**, *19*, 1735. (e) Enemark, J. H.; Feltham, R. D. *Coord. Chem. Rev.* **1974**, *13*, 339. (f) Connelly, N. G. *Inorg. Chim. Acta Rev.* **1972**, *6*, 47. (g) Frenz, B. A.; Ibers, J. A. *M. T. P. Int. Rev. Sci. Phys. Chem. Ser. One* **1972**, *11*, 33. (h) Griffith, W. P. *Adv. Organomet. Chem.* **1968**, *7*, 211.

0002-7863/92/1514-1970$03.00/0

Chart I

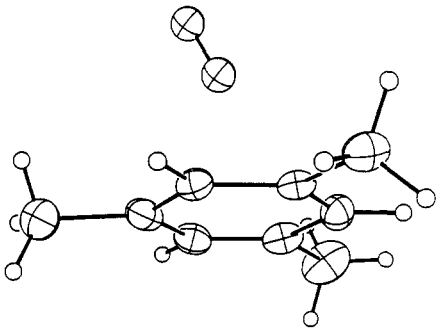

high electron affinity (EA = 9.26 eV)[5] and reversible reduction potential of E_{red}^0 = 1.28 V.[6] For example, the ambivalent behavior of NO^+ toward different aromatic donors (Ar) is illustrated by the ready one-electron oxidation of anthracene to the anthracene cation radical,[7] i.e.

$$Ar + NO^+ \rightarrow Ar^{\bullet+} + NO \quad (1)$$

as compared to the rapid formation of a persistent electron donor–acceptor or EDA complex with benzene (eq 2).[8,9] The latter

$$Ar + NO^+ \rightleftharpoons [Ar,NO^+] \quad (2)$$

is of particular interest since X-ray crystallography of such intermolecular complexes of arenes with NO^+ salts has established the centrosymmetric (η^6) structure[10] illustrated in the ORTEP diagram in Chart I for the mesitylene derivative.[11] In the 1:1 molecular complex, the closest approach of NO^+ to an aromatic carbon of 2.5 Å exceeds the distance for conventional bonding, and it is determined solely by charge-transfer (CT) interactions of the type described by Mulliken.[12,13]

Nitrosonium is also an unique cation, being the only strong diatomic oxidant known to be capable of a chemically reversible redox change in a reasonably accessible potential range of E_{red}^0 = 1.28 V vs SCE.[14,15] Moreover the one-electron redox couple, i.e.

$$NO^+ + \epsilon \overset{E_{red}^0}{\rightleftharpoons} NO \quad (3)$$

generates the paramagnetic nitric oxide that is well-behaved in solution owing to its limited tendency for dimerization.[16] By comparison, the related triatomic cation NO_2^+ undergoes the reversible redox change at a similar potential of E_{red}^0 = 1.32 V vs SCE,[17] but it affords nitrogen dioxide that is subject to extensive dimerization,[18] i.e.

$$NO_2^+ + \epsilon \overset{E_{red}^0}{\rightleftharpoons} NO_2 \overset{K}{\rightleftharpoons} N_2O_4 \quad (4)$$

The dual capacity of the nitrosonium cation to effect oxidation readily (eq 1) and to form charge-transfer complexes efficiently (eq 2)[19] is particularly important to the kinetics study of both thermal and photoinduced processes for electron transfer.[20,21] Thus recent time-resolved picosecond spectroscopic experiments have identified the charge-transfer excitation ($h\nu_{CT}$) of aromatic EDA complexes with various types of electron acceptors (A),[21-26] i.e.

$$Ar + A \rightleftharpoons [Ar,A] \overset{h\nu_{CT}}{\underset{k_1}{\rightleftharpoons}} [Ar^{\bullet+},A^{\bullet-}] \quad (5)$$

However the back electron transfer from the ion radical *pair* by first-order kinetics (k_1) is the dominant relaxation pathway observed heretofore.[27] The alternative path that follows second-order kinetics resulting from electron transfer between the *free* ions (after their diffusive separation from the ion radical pair) is unreported.[30] Since the second-order kinetics also relate directly to the dynamics of thermal (adiabatic) electron transfer (k_{ET}),[31] the competition between back electron transfer (k_1) and diffusive separation (k_s) of the photogenerated ion radical pairs,[32] i.e.

$$[Ar,A] \overset{k_1}{\longleftarrow} [Ar^{\bullet+},A^{\bullet-}] \overset{k_s}{\underset{k_s}{\rightleftharpoons}} Ar^{\bullet+} + A^{\bullet-} \quad (6)$$

(3) (a) Johnson, B. F. G.; Segal, J. A. *J. Organomet. Chem.* **1971**, *31*, C79. (b) Johnson, B. F. G.; Bhaduri, S.; Connelly, N. G. *J. Organomet. Chem.* **1972**, *40*, C36. (c) Fitzgerald, R. J.; Lin, H. M. W. *Inorg. Chem.* **1972**, *11*, 2270. (d) Connelly, N. G.; Dahl, L. F. *J. Chem. Soc., Chem. Commun.* **1970**, 880. (e) Simpson, J. M.; Kapp, D. C.; Chapman, T. M. *Synthesis* **1979**, 100. (f) Marvel, C. S.; Porter, P. K. *Org. Synth. Collect.* **1941**, *I (Collect. Vol)*, 411. (g) Challis, B. C.; Lawson, A. J. *J. Chem. Soc., Perkin Trans. II* **1973**, 918.

(4) (a) Musker, W. K.; Wolfold, T. L.; Roush, P. B. *J. Am. Chem. Soc.* **1978**, *100*, 6416. (b) Eberson, L.; Radner, F. *Acta Chem. Scand.* **1984**, *B38*, 861. (c) Bandlish, B. K.; Shine, H. J. *J. Org. Chem.* **1977**, *42*, 561. (d) Reimann, R. H.; Singleton, E. *J. Organomet. Chem.* **1971**, *32*, C44. (e) Connelly, N. G.; Davies, J. D. *J. Organomet. Chem.* **1972**, *38*, 385. (f) Bock, H.; Brähler, G.; Henkel, U.; Schlecker, R.; Seebach, D. *Chem. Ber.* **1980**, *113*, 289. (g) Kosechko, V. G.; Inozemtsev, A. N.; Pokhodenko, V. D. *Zh. Org. Khim.* **1981**, *17*, 2608.

(5) Albritton, D. L.; Schmeltekopf, A. L.; Zare, R. N. *J. Chem. Phys.* **1979**, *71*, 3271.

(6) Lee, K. Y.; Kuchynka, D. J.; Kochi, J. K. *Inorg. Chem.* **1990**, *29*, 4196.

(7) Kim, E. K.; Kochi, J. K. *J. Org. Chem.* **1989**, *54*, 1692.

(8) Reents, W. D., Jr.; Freiser, B. S. *J. Am. Chem. Soc.* **1980**, *102*, 271.

(9) Brownstein, S.; Gabe, E.; Lee, F.; Tan, L. *J. Chem. Soc., Chem. Commun.* **1984**, 1566.

(10) Brownstein, S.; Gabe, E.; Lee, F.; Piotrowski, A. *Can. J. Chem.* **1986**, *64*, 1661.

(11) See the following for a preliminary report: Kochi, J. K. *Pure Appl. Chem.* **1991**, *63*, 255.

(12) Mulliken, R. S. *J. Am. Chem. Soc.* **1950**, *72*, 600.

(13) Mulliken, R. S.; Person, W. B. *Molecular Complexes*; Wiley: New York, 1969.

(14) Lee, K. Y.; Kuchynka, D. J.; Kochi, J. K. In ref 6. See also: Boughriet, A.; Wartel, M. *J. Chem. Soc., Chem. Commun.* **1989**, 809.

(15) Although the $O_2^+ \rightleftharpoons O_2$ couple is likely to be reversible, the value of $E \sim 5$ V is outside the potential range for use with most solvents. (See: Dinnocenzo, J. P.; Banach, T. E. *J. Am. Chem. Soc.* **1986**, *108*, 6063.)

(16) Bontempelli, G.; Mazzocchin, G. A.; Magno, F. *Electroanal. Chem. Interfac. Electrochem.* **1974**, *55*, 91. See also: Fateley, W. G.; Bent, H. A.; Crawford, B., Jr. *J. Chem. Phys.* **1958**, *64*, 204. Dinerman, C. E.; Ewing, G. E. *J. Chem. Phys.* **1970**, *53*, 626.

(17) Lee, K. Y.; Amatore, C.; Kochi, J. K. *J. Phys. Chem.* **1991**, *95*, 1285.

(18) (a) Vosper, A. J. *J. Chem. Soc. A* **1970**, 2191. (b) James, D. W.; Marshall, R. C. *J. Phys. Chem.* **1968**, *72*, 2963. (c) Addison, C. C. *Chem. Rev.* **1980**, *80*, 21.

(19) Kim, E. K.; Kochi, J. K. *J. Am. Chem. Soc.* **1991**, *113*, 4962.

(20) See, e.g.: Eberson, L. *Electron Transfer Reactions in Organic Chemistry*; Springer: New York, 1987.

(21) Jones, G., II In *Photoinduced Electron Transfer*, Part A; Fox, M. A., Chanon, M., Eds.; Elsevier: New York, 1988; p 245 ff.

(22) (a) Masuhara, H.; Shimada, M.; Tsujino, N.; Mataga, N. *Bull. Chem. Soc. Jpn.* **1971**, *44*, 3310. (b) Masuhara, H.; Shimada, M.; Mataga, N. *Bull. Chem. Soc. Jpn.* **1970**, *43*, 3316. (c) Mataga, N.; Kanda, Y.; Okada, T. *J. Phys. Chem.* **1986**, *90*, 3880.

(23) (a) Hilinski, E. F.; Masnovi, J. M.; Amatore, C.; Kochi, J. K.; Rentzepis, P. M. *J. Am. Chem. Soc.* **1983**, *105*, 6167. (b) Rentzepis, P. M.; Steyert, D. W.; Roth, H. D.; Abelt, C. J. *J. Phys. Chem.* **1985**, *89*, 3955.

(24) (a) Jones, G., II; Haney, W. A.; Phan, X. T. *J. Am. Chem. Soc.* **1988**, *110*, 1922. (b) Jones, G., II; Mouli, N. *J. Phys. Chem.* **1988**, *92*, 7174. (c) Ebbesen, T. W.; Manring, L. E.; Peters, K. S. *J. Am. Chem. Soc.* **1984**, *106*, 7400. (d) Atherton, S. J.; Hubig, S. M.; Callan, T. J.; Duncanson, J. A.; Snowden, P. T.; Rodgers, M. A. J. *J. Phys. Chem.* **1987**, *91*, 3137.

(25) (a) Mataga, N.; Shioyama, H.; Kanda, Y. *J. Phys. Chem.* **1987**, *91*, 314. (b) Kobashi, H.; Funabashi, M.; Shizuka, H.; Okado, T.; Mataga, N. *Chem. Phys. Lett.* **1989**, *160*, 261. (c) Miyasaka, H.; Ojima, S.; Mataga, N. *J. Phys. Chem.* **1989**, *93*, 3380. (d) Ojima, S.; Miyasaka, H.; Mataga, N. *J. Phys. Chem.* **1990**, *94*, 4147, 5834, 7534.

(26) (a) Gould, I. R.; Ege, D.; Mattes, S. L.; Farid, S. *J. Am. Chem. Soc.* **1987**, *109*, 3794. (b) Gould, I. R.; Ege, D.; Moser, J. E.; Farid, S. *J. Am. Chem. Soc.* **1990**, *112*, 4290. (c) Gould, I. R.; Moser, J. E.; Armitage, B.; Farid, S. *J. Am. Chem. Soc.* **1989**, *111*, 1917. (d) Gould, I. R.; Moody, R.; Farid, S. *J. Am. Chem. Soc.* **1988**, *110*, 7242. (e) Gould, I. R.; Young, R. H.; Moody, R. E.; Farid, S. *J. Phys. Chem.* **1991**, *95*, 2068.

(27) Temporal relaxation of the first-formed ions as the contact ion pairs to the solvent-separated ion pairs[28] as well as various fragmentations, rearrangements, etc.[29] are also to be included among other first-order processes.

(28) Goodman, J. L.; Peters, K. S. *J. Am. Chem. Soc.* **1985**, *107*, 1441, 6459; **1986**, *108*, 1700; *J. Phys. Chem.* **1986**, *90*, 5506. See also: O'Driscoll, E.; Simon, J. D.; Peters, K. S. *J. Am. Chem. Soc.* **1990**, *112*, 7091.

(29) Tatikolov, A.; Yang, X.; Sauerwein, B.; Schuster, G. B. *Acta Chem. Scand.* **1990**, *44*, 837. For a review, see: Saeva, F. D. *Top. Curr. Chem.* **1990**, *156*, 59.

(30) First- and second-order kinetics accompanying photoinduced electron transfer have been observed in dissociative charge-transfer processes (Masnovi, J. M.; Kochi, J. K. *J. Am. Chem. Soc.* **1985**, *107*, 7880). See also: Pienta, N. J.; Kessler, R. J.; Peters, K. S.; O'Driscoll, E. D.; Arnett, E. M.; Molter, K. E. *J. Am. Chem. Soc.* **1991**, *113*, 3773.

(31) See for example: Cannon, R. D. *Electron-Transfer Reactions*; Butterworths: Boston, 1980.

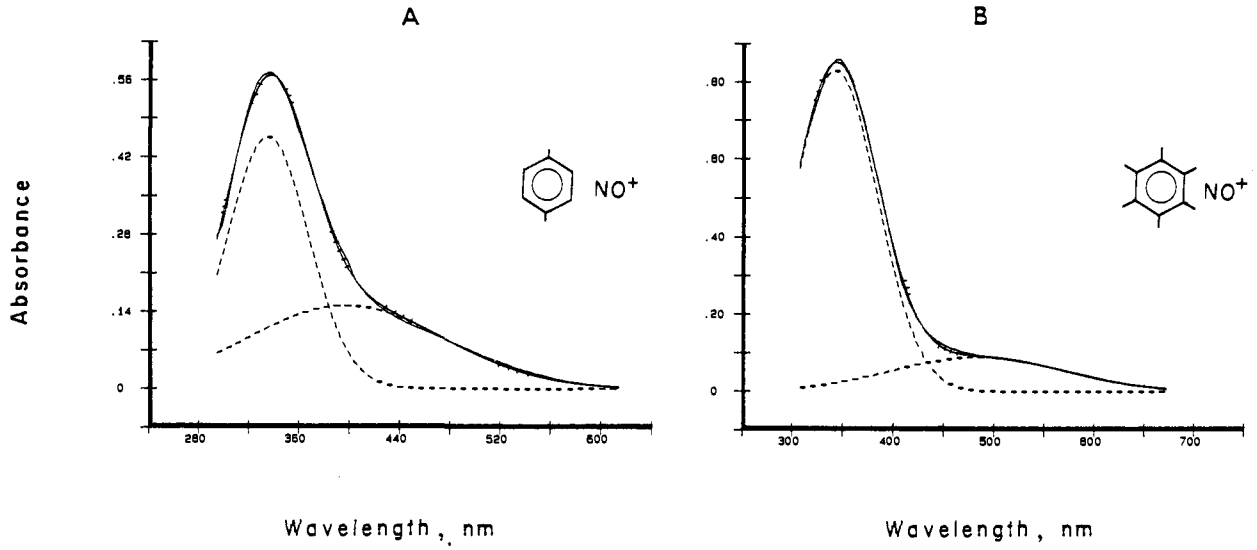

Figure 1. Charge-transfer absorption spectrum of the NO^+ complex with (A) *p*-xylene and (B) hexamethylbenzene (—) in acetonitrile, showing the computer fit (–++–) based on the Gaussian deconvolution (---) into CT bands A and B.

must be addressed explicitly. The availability of the aromatic EDA complexes with nitrosonium cation, we believe, presents a unique opportunity to examine the complete electron-transfer kinetics (summarized by eqs 5 and 6) for the following reasons. First, the comparable magnitudes of the ionization potentials[33] of benzene (IP = 9.23 eV) and nitric oxide (IP = 9.26 eV) ensure that minimal driving forces pertain to electron transfer in either direction, i.e.[34]

$$C_6H_6 + NO^+ \rightleftharpoons C_6H_6^{\bullet+} + NO \qquad (7)$$

As such, the detailed microdynamics for electron-transfer mechanisms of reactive species (such as the aromatic radical ion in eq 7) can be examined in the *isoergonic* region of the free energy change.[35] Second, the diffusive separation of the ion radical pairs with net (positive) charge is relatively unrestrained by the Coulombic attraction inherent to CT ion pairs produced by the photoexcitation of neutral donor–acceptor pairs.[36] Most important for the kinetics study is the controlled amounts of nitric oxide that can be deliberately added to modulate the electron-transfer kinetics without complications from the dimer equilibrium. Accordingly, we proceed in this study with the description of a graded series of aromatic complexes with NO^+ in solution that is followed by time-resolved spectroscopic studies to encompass the time span of six decades for the examination of the spectral characteristics and the kinetics behavior of the ion radical pair $[Ar^{\bullet+},NO]$ as they evolve from the initial charge-transfer excitation.

Results

I. Formation of Charge-Transfer Complexes of Aromatic Donors with Nitrosonium Salts in Solution. The addition of benzene and other alkylbenzenes to a dilute solution of the nitrosonium salt ($NO^+BF_4^-$, $NO^+PF_6^-$, $NO^+SbF_6^-$, or $NO^+SbCl_6^-$) in acetonitrile resulted in the spontaneous development of a bright yellow to dark red-brown color that was markedly dependent on the aromatic donor. [Since the counterion had no effect on the visual changes observed in solution, it will be omitted from the presentation hereafter.] Such intense colors were accompanied by the appearance of a pair of absorption bands in the electronic spectra—a strong band with λ_{max} lying in region A, 320/360 nm, and a weaker, low-energy band usually appearing as a broad shoulder in region B, 400/700 nm. The Gaussian (digital) deconvolution of the absorption spectra in Figure 1 typically illustrates the resolution of the charge-transfer bands A and B from acetonitrile solutions of the NO^+ complexes with *p*-xylene and hexamethylbenzene. Similar spectra were observed in dichloromethane and nitromethane, and the spectrophotometric analysis based on the Benesi-Hildebrand relationship[37,38] yielded the formation constants (K_{EDA}) and the extinction coefficients (ϵ_{CT}) of the 1:1 charge-transfer complexes, i.e.

$$Ar + NO^+ \overset{K_{EDA}}{\rightleftharpoons} [Ar,NO^+] \qquad (8)$$

from the series of aromatic donors listed in Table I.[19]

For comparative purposes, the crystalline 1:1 charge-transfer complexes of $NO^+PF_6^-$ with the aromatic donors mesitylene, durene, pentamethylbenzene, and hexamethylbenzene were isolated from dichloromethane solutions by crystallization at −20 °C. Since the diffuse reflectance spectra of these crystalline complexes were essentially the same as the absorption spectra obtained in solution (Table I),[19] the centrosymmetric structure (see Chart I), as established by X-ray crystallography,[10] can also be taken to represent the structures of the $[Ar,NO^+]$ complexes extant in solution.

II. Thermal Stability and Photostability of the Charge-Transfer Complexes in Solution. The charge-transfer complexes of benzene and toluene with NO^+ persisted in acetonitrile for prolonged periods at room temperature when the solutions were carefully protected from moisture and air.[7] Charge-transfer complexes from the more electron-rich arenes such as hexamethylbenzene and durene were less stable, and the solutions evolved minor amounts of nitric oxide over the course of several hours, presumably as a result of the slow oxidation of the arene donor.[19] Traces of NO also arose from the inevitable hydrolysis of the hygroscopic nitrosonium salts[39] from adventitious moisture—even when extra precautions were taken to prepare all the solutions in a controlled, dry environment.[40] Fortunately the small quantities of nitric oxide in solution could be precisely assayed by steady-state voltammetry with the aid of platinum microelectrodes in the absence of any supporting electrolyte, as described in detail in the Experimental

(32) The electron-transfer rate constant is related to the microdynamical rate constants k_1, k_s, and k_a in eq 6 by the following relationship: $k_{ET} = k_1k_a/(k_1 + k_s)$ for the steady-state situation in which $k_1, k_s \gg k_a[NO]$ and $k_{ET} = k_1k_a/k_s$ for the equilibrium situation in which $k_s > k_1$. For the exact relationship, see the Appendix.

(33) (a) Howell, J. O.; Goncalves, J. M.; Amatore, C.; Klasinc, L.; Wightman, R. M.; Kochi, J. K. *J. Am. Chem. Soc.* **1984**, *106*, 3968. (b) Lias, S. G. *Chem. Phys. Lett.* **1978**, *54*, 147.

(34) For the comparable processes in solution, the solvation of the cationic species (NO^+)[6] and (Ar^+)[33] must be included.

(35) By contrast, all the systems heretofore examined by time-resolved spectroscopy[22-26] involve electron transfers that lie in the strongly exergonic region of the free energy change.

(36) See: Eberson, L. in ref 20, Table 1 (p 34).

(37) Benesi, H. A.; Hildebrand, J. H. *J. Am. Chem. Soc.* **1949**, *71*, 2703.

(38) Person, W. B. *J. Am. Chem. Soc.* **1965**, *87*, 167.

(39) Cotton, F. A.; Wilkinson, G. ref 1, p 323.

(40) Vacuum Atmospheres HE-493 glovebox with <2 ppm water.

Table I. Charge-Transfer Complexes of Aromatic Donors with Nitrosonium Salts[a]

arene	IP (eV)	$h\nu_{CT}$(A) (eV/10^2 cm^{-1})[b]	$h\nu_{CT}$(B) (eV/10^3 cm^{-1})[b,c]	K_{EDA} (M^{-1})	ϵ_{CT} (M^{-1} cm^{-1})[d]
benzene	9.23	3.61 (85)	3.1 (6)	0.5	800 (60)
chlorobenzene	9.08	3.62 (92)	3.1 (6)	2.0	100 (6)
bromobenzene	9.05	3.82 (85)	3.1 (8)		
toluene	8.82	3.70 (93)	2.6 (5)	5.0	400 (–)
tert-butylbenzene	8.65	3.59 (80)	2.8 (5)	7.0	270 (50)
o-xylene	8.56	3.64 (77)	2.8 (6)	30	2200 (200)
p-xylene	8.44	3.65 (69)	2.4 (6)	30	1300 (80)
mesitylene	8.42	3.55 (76)	2.6 (5)	55	2100 (–)
durene	8.05	3.67 (71)	2.6 (5)	450	1100 (40)
pentamethylbenzene	7.92	3.70 (70)	2.5 (5)	5000	2400 (–)
hexamethylbenzene	7.85	3.64 (71)	2.5 (6)	31000	3100 (–)
1,2-DNP[e]	7.66	3.63 (80)	2.4 (5)		
1,4-DNP[e]	7.71	3.30 (50)	2.4 (5)		

[a] With 10^{-3} M $NO^+BF_4^-$ and excess arene in acetonitrile at 25 °C from ref 19. [b] Bandwidth (fwhm) in parentheses. [c] By Gaussian (digital) deconvolution. [d] Band A (band B). [e] Dineopentyltetramethylbenzene.

Section. Most importantly, the microvoltammetric method of analysis also allowed the NO levels to be accurately and rapidly monitored subsequent to the measured introduction of nitric oxide into solutions of the EDA complexes.

The deliberate irradiation of the charge-transfer complexes with the output from a 1 kW xenon lamp passed through a Pyrex filter (cutoff $\lambda < 320$ nm) did not lead to any permanent photochemical transformation since the charge-transfer spectrum was unchanged and the benzene donor could be quantitatively recovered intact. Furthermore, no spectral changes were observed during the steady-state photoexcitation of the charge-transfer complexes of NO^+ with *o*-xylene, durene, pentamethylbenzene, and hexamethylbenzene; and after prolonged irradiation (1–2 h) the workup of the photolysate led to the quantitative recovery of the arene donors (see Experimental Section). Accordingly, we were assured that all the spectral transients observed during the following time-resolved spectroscopic studies eventually decayed completely back to the ground-state complex [Ar,NO^+] unchanged.

III. Time-Resolved Nanosecond Spectroscopic Studies of [Ar,NO^+] Complexes. To identify the reactive intermediates in the charge-transfer excitation of the [Ar,NO^+] complexes in solution, we initially examined the time-resolved spectra of the transients following the application of a 10-ns (fwhm) laser pulse. The second harmonic at 532 nm of the Q-switched Nd^{3+}:YAG laser was used to excite the charge-transfer bands of the NO^+ complexes with hexamethylbenzene (HMB), pentamethylbenzene (PMB), and durene (DUR) in acetonitrile solutions. The spectral window in the nanosecond measurements enabled the absorption spectra of the CT transients to be examined between 300 and 1050 nm. The difference transient spectra obtained from the excitation of the [Ar,NO^+] complexes revealed the pronounced negative absorption ($\Delta A < 0$) in the spectral region 300/420 nm that corresponded to the bleaching of the ground-state CT complex (see the listings of the CT band A in Table I). Typically, the depletion of the hexamethylbenzene complex of NO^+ in Figure 2 (as shown by the negative absorbance centered at $\lambda_{CT} = 335$ nm) was accompanied by the concomitant appearance of the hexamethylbenzene cation radical ($HMB^{\bullet+}$) with the positive absorbance ($\Delta A > 0$) centered at $\lambda_{max} = 492$ nm. The subsequent disappearance of $HMB^{\bullet+}$ is shown in Figure 2 by the return of the difference absorbances back to the baseline within a few microseconds. The transient spectra obtained from the CT excitation of solutions containing either equimolar amounts of HMB and $NO^+BF_4^-$ or a 5-fold excess of either component were all the same, and the spectra thus showed no effects on concentration. The latter stems from the large magnitude of the formation constant K_{EDA} in Table I, and it accords with the direct excitation of the charge-transfer complex, i.e.

$$[Ar,NO^+] \xrightarrow{h\nu_{CT}} [Ar^{\bullet+},NO] \qquad (9)$$

The accompanying presence of nitric oxide in eq 9 was not observed in the transient spectrum owing to its predominant absorption at $\lambda < 230$ nm.[41] However, the co-production of NO

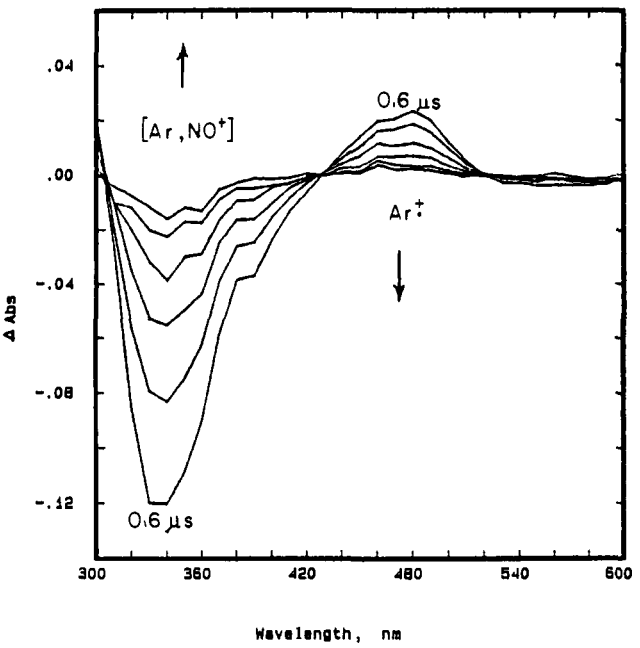

Figure 2. Temporal decay of the hexamethylbenzene cation radical ($Ar^{\bullet+}$) and the simultaneous recovery of the charge-transfer band of [Ar,NO^+] at 0.6, 1.4, 2.7, 4.4, 6.5, and 8.7 μs following the application of the 10-ns pulse at 355 nm to a solution of 2 mM hexamethylbenzene (Ar) and 0.8 mM $NO^+BF_4^-$ in acetonitrile.

is demanded by the stoichiometry and the absence of any photochemical reaction attendant upon the prolonged irradiation of the CT absorption band (vide supra).

Similarly, the 532-nm excitation of the NO^+ complexes of pentamethylbenzene and durene as well as the hindered 1,2-, 1,3-, and 1,4-dineopentyltetramethylbenzenes (DNP) with the 10-ns pulse also led to the negative absorption in the region 400/460 nm due to the bleaching of the CT bands and the positive absorption in the region 460/700 nm with maxima at 485, 460, 520, 520, and 540 nm respectively, of the arene cation radicals $PMB^{\bullet+}$, $DUR^{\bullet+}$, and $DNP^{\bullet+}$, respectively. The latter were the same as those previously generated independently[42] or from the CT excitation of these arene complexes with tetranitromethane in acetonitrile.[43]

(41) Jones, K. *Comprehensive Inorganic Chemistry*; Bailar, J. C., Jr., Emeleus, H. J., Nyholm, R., Trotman-Dickenson, A. F., Eds.; Pergamon: Oxford, 1973; Vol. 2, p 237. Heicklen, J.; Cohen, N. In *Advances in Photochemistry*; Noyes, W. A., Jr., Hammond, G. S., Pitts, J. N., Jr., Eds.; Interscience: New York, 1968; Vol. 5, pp 157–328.

(42) Masnovi, J. M.; Sankararaman, S.; Kochi, J. K. *J. Am. Chem. Soc.* **1989**, *111*, 2263.

(43) Masnovi, J. M.; Kochi, J. K.; Hilinski, E. F.; Rentzepis, P. M. *J. Am. Chem. Soc.* **1986**, *108*, 1126.

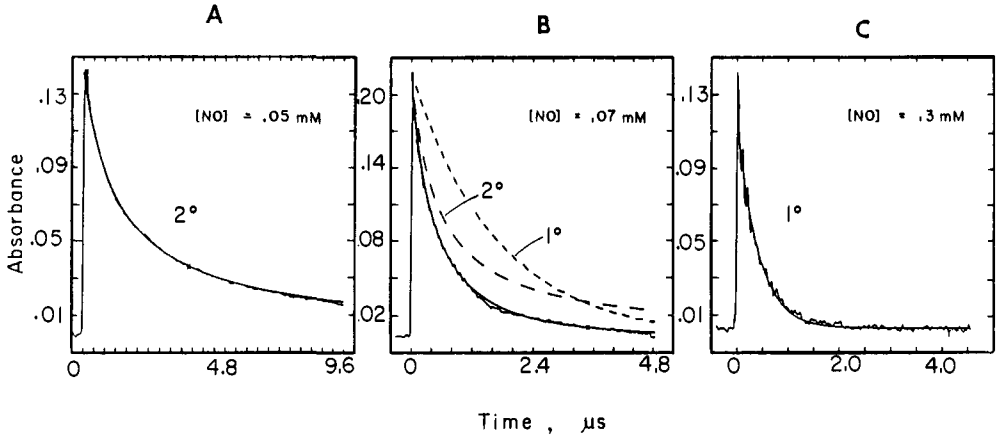

Figure 3. Variation in the decay kinetics of $HMB^{\bullet+}$, monitored at λ_{max} = 490 nm following the application of the 10-ns pulse at 532 nm to a solution of 3 mM HMB and 1 mM $NOBF_4$ in nitromethane at 25 °C containing (A) 0.05, (B) 0.07, and (C) 0.30 mM nitric oxide. The smooth curves show the computer fits of the second-order (2°), composite (2° and 1°), and first-order (1°) kinetics.

In order to examine the spectral transients of the NO^+ complexes with the weaker arene donors, such as benzene and toluene, they were irradiated with the third harmonic 355-nm pulse from the Q-switched Nd^{3+}:YAG laser by exploiting the larger transition moments of the high-energy CT bands A (compare columns 8 and 9 in Table I). For example, the time-resolved nanosecond spectrum obtained by the excitation of a solution of 25 mM benzene and 50 mM $NO^+BF_4^-$ in acetonitrile consisted of a well-resolved visible band with λ_{max} = 430 nm in excellent agreement with that of the benzene cation radical ($BZ^{\bullet+}$) reported previously.[44] The same procedure afforded the transient spectra of the cation radicals derived from various aromatic donors, including *p*-xylene, toluene, and other polymethylbenzenes together with biphenyl and chloro-, bromo-, and iodobenzene.[45-55] The spectral comparison of the aromatic cation radicals in Table II with those previously based on pulse[45] or γ-radiolysis,[46,47] photodissociation,[44] flash photolysis,[55] and by theoretical calculation[49] (column 6) established the experimental viability of the CT excitation of [Ar,NO^+] complexes to probe a wide variety of structures. For example, the progressive bathochromic (red) shift of the visible band (λ_{max} = 430 nm) for benzene cation radical with increasing number of methyl substituents to 490 nm for $HMB^{\bullet+}$ relates to the theoretical basis for the "methyl effect".[56,57] Among the halobenzenes, the red shift in the absorption band of the cation radicals from chlorobenzene (470 nm), bromobenzene (540 nm), and iodobenzene relative to the benzene cation radical followed the expected trend arising from the strongly allowed (n → π*) charge-transfer transition.[50,52] All the transient spectra were rather insensitive to variations of solvent polarity, the same series of spectra being obtained in such nonpolar solvents as dichloromethane and nitromethane.

Table II. Formation of Aromatic Cation Radicals by Charge-Transfer Excitation[a]

arene	arene concn (mM)	$NO^+BF_4^-$ (mM)	λ_{exc}[b] (nm)	λ_{max}[c,d] (nm)
benzene	25	50	355	430 (427)[e,f]
chlorobenzene	200	50	355	470 (470)[g,h]
bromobenzene	200	50	355	540 (565)[g,h]
iodobenzene	130	100	532	680 (625)[i]
toluene	16	25	355	430 (430)[j,k]
ethylbenzene	16	20	355	445
cumene	16	20	355	450 (505)[i]
tert-butylbenzene	300	13	532	470 (547)[i]
o-xylene	8	10	355	435 (433)[e,k]
p-xylene	7	8	355	440 (435)[e,k]
	15	8	532	440
prehnitene	15	8	532	455 (445)[e,k]
durene	10	20	355	460 (465)[e,k]
	13	6	532	460
pentamethylbenzene	2	1	355	485 (475)[e,k]
	0.6	4	532	490
hexamethylbenzene	2	1	355	490 (500)[e,k]
	1.5	2	532	490
1,2-DNP[m]	5	5	532	520
1,4-DNP[m]	2.5	2.5	532	540
biphenyl	24	25	355	660 (690)[l]
	65	100	532	670

[a] In acetonitrile at 25 °C. [b] Excitation wavelength. [c] Absorption maximum of the arene cation radical. [d] Value in parentheses from the reference cited. [e] Reference 44a. [f] Reference 44e. [g] Reference 50. [h] Reference 52. [i] Reference 53. [j] Reference 51. [k] Reference 45. [l] Reference 55. [m] DNP = dineopentyltetramethylbenzene.

IV. Temporal Evolution of Long-Lived Aromatic Cation Radicals in Solution. The spectral transients of aromatic cation radicals in Table II persisted in solution for relatively prolonged periods—certainly by comparison with those generated by other methods.[45-55] Thus the absorbance of $Ar^{\bullet+}$ followed at λ_{max} (Table II) was essentially unchanged in the time span from 50 to 100 ns following the CT excitation, more or less independent of the aromatic donor. The quantum efficiency for the production of the aromatic cation radical via the excitation of the CT complex within this interval was evaluated by the method of relative actinometry.[58] The actinometers for the 355- and 532-nm excitations were based on the benzophenone triplet with λ_{max} = 530 nm (Φ_T = 1.0 and ϵ_T = 7220 M^{-1} cm^{-1})[59] and hematoporphyrin

(44) (a) Dymerski, P. P.; Fu, E.; Dunbar, R. C. *J. Am. Chem. Soc.* **1974**, *96*, 4109. (b) Dunbar, R. C. *Chem. Phys. Lett.* **1975**, *32*, 508. (c) Dunbar, R. C.; Klein, R. *J. Am. Chem. Soc.* **1976**, *98*, 7994. (d) Dunbar, R. C. *Anal. Chem.* **1976**, *48*, 723. See also: (e) Carlson, T. A.; Anderson, C. P. *Chem. Phys. Lett.* **1971**, *10*, 561. (f) Marschner, F.; Goetz, H. *Tetrahedron* **1974**, *30*, 3451. Marschner, F. *Tetrahedron* **1975**, *31*, 2303.

(45) Sehested, K.; Holcman, J.; Hart, E. J. *J. Phys. Chem.* **1977**, *81*, 1363.

(46) (a) Miller, J. H.; Andrews, L.; Lund, P. A.; Schatz, P. N. *J. Chem. Phys.* **1980**, *73*, 4932. (b) Andrews, L.; Keelan, B. W. *J. Am. Chem. Soc.* **1980**, *102*, 5732.

(47) (a) Shida, T.; Hamill, W. H. *J. Chem. Phys.* **1966**, *44*, 2369, 4372. (b) Shida, T.; Kato, T. *Chem. Phys. Lett.* **1979**, *68*, 106.

(48) Teng, H. H.; Dunbar, R. C. *J. Chem. Phys.* **1978**, *68*, 3133. See also refs 63 and 42.

(49) Gardner, C. L. *J. Chem. Phys.* **1966**, *45*, 572.

(50) Keelan, B. W.; Andrews, L. *J. Am. Chem. Soc.* **1981**, *103*, 829.

(51) Andrews, L.; Miller, J. H.; Keelan, B. W. *Chem. Phys. Lett.* **1980**, *71*, 207.

(52) Dunbar, R. C.; Teng, H. H.; Fu, E. *J. Am. Chem. Soc.* **1979**, *101*, 6506.

(53) Fritz, H. P.; Gebauer, H. *Z. Naturforsch.* **1978**, *33b*, 702.

(54) Szymanska-Buzar, T.; Ziolkowski, J. J. *J. Mol. Catal.* **1979**, *5*, 341.

(55) Vauthey, E.; Suppan, P.; Haselbach, E. *Helv. Chim. Acta* **1988**, *71*, 93.

(56) Heilbronner, E.; Maier, J. P. In *Photoelectron Spectroscopy*; Brundle, C. R., Baker, A. D., Eds.; Academic: New York, 1977; Vol. 1, p 205 ff. See also: Heilbronner, E.; Hoshi, T.; von Rosenberg, J. L.; Hafner, K. *Nouv. J. Chem.* **1977**, *1*, 105.

(57) Lau, W.; Kochi, J. K. *J. Am. Chem. Soc.* **1986**, *108*, 6720.

(58) (a) Carmichael, I.; Hug, C. L. *J. Phys. Chem. Ref. Data* **1986**, *15*, 15. (b) Amand, B.; Bensasson, R. *Chem. Phys. Lett.* **1975**, *34*, 44.

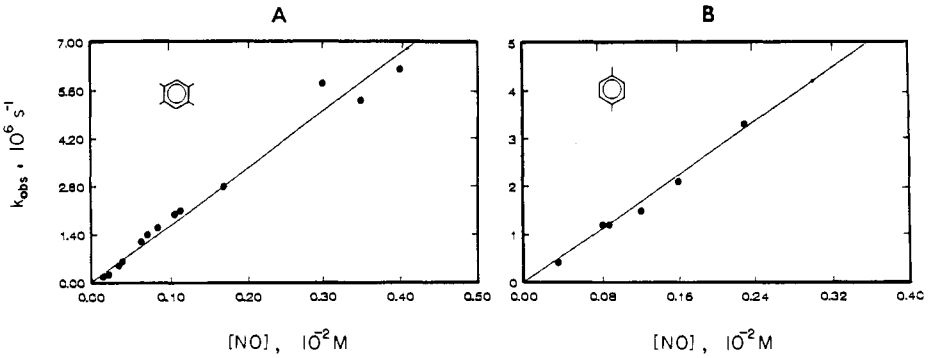

Figure 4. The dependence of the experimental first-order rate constant k_{obs} from (A) durene and (B) *p*-xylene on the concentration of nitric oxide in acetonitrile. The smooth line is fitted to eq 19, as described in the Experimental Section.

Table III. Quantum Efficiency for the Formation of Aromatic Cation Radicals by CT Excitation[a]

aromatic donor	solvent	actinometer[b]	λ_{exc}	λ_{mon}	Φ[c]
hexamethylbenzene	CH_3CN	BP	355	490	0.70 ± 0.04 (0.70)
	CH_3CN	HP	532	490	0.68 ± 0.03
	CH_3NO_2	HP	532	490	0.70 ± 0.04 (0.68)
pentamethylbenzene	CH_3CN	HP	532	480	0.60 ± 0.05 (0.60)
durene	CH_3CN	BP	355	460	0.44 ± 0.04 (0.46)
	CH_3NO_2	HP	532	460	0.36 ± 0.1 (0.25)
p-xylene	CH_3CN	BP	355	440	0.39 ± 0.04 (0.42)
	CH_3CN	HP	532	440	0.40 ± 0.05
	CH_3NO_2	HP	532	440	0.10 ± 0.1 (0.08)

[a] In solutions containing 15 mM Ar and 5 mM $NO^+BF_4^-$ at 25 °C. [b] BP = benzophenone, HP = hematoporphyrin IX. [c] Quantum yield (±0.1) for the formation of $Ar^{\bullet+}$ at λ_{mon} at 50 ns following 10-ns laser pulse excitation at λ_{exc} with the standard deviation of the measurement. Value in parentheses calculated from the graphical fit (see Experimental Section).

IX with λ_{max} = 460 nm (Φ_T = 0.82 and $\Delta\epsilon_T$ = 10400 M^{-1} cm^{-1}),[60] respectively, as fully described in the Experimental Section. The results included in Table III show that the hexamethylbenzene cation radical was consistently generated (in the 50–100-ns window) with reasonable efficiency, the quantum yield Φ = 0.7 being independent of the solvent (acetonitrile and nitromethane) and the excitation energy (λ_{exc} = 355 and 532 nm). However, the marked dependence on the aromatic donor is shown (column 6) by the sharp dropoff of the quantum yields for the production of $DUR^{\bullet+}$ and $XYL^{\bullet+}$ from the durene and *p*-xylene complexes to 0.4 and 0.1, respectively.

V. Spectral Decay of $Ar^{\bullet+}$ by Second-Order Kinetics and the Effect of Added Nitric Oxide. By the continued monitoring of the absorbance change, the spectral decay of the aromatic cation radical was found to eventually fall back to the baseline in the time interval lasting up to several microseconds. Most significantly, the decay profile was *strongly* dependent on the concentration of nitric oxide in solution. The effect of nitric oxide on the kinetics was best illustrated in nitromethane solutions since the NO level could be controlled most readily in this medium. Thus Figure 3 shows the graphical fit of the spectral decays of hexamethylbenzene cation radical successively to (a) second-order, (b) mixed second-/first-order, and (c) first-order kinetics that follow the gradual increase in nitric oxide concentration from 5.0 × 10^{-5}, to 7.0 × 10^{-5}, to 3.0 × 10^{-4} M, respectively. It is important to emphasize that the changes in the decay profiles shown in Figure 3 were *completely reversible*—the deliberate addition of extra nitric oxide to the solution in Figure 3A resulting in the behavior shown in Figure 3C, and conversely, the behavior in Figure 3C reverting to that shown in Figure 3A by the careful entrainment of nitric oxide from the solution with the aid of a stream of dry argon, and so forth.

Table IV. Effect of Nitric Oxide on the Decay Kinetics of Long-Lived Aromatic Cation Radicals[a]

aromatic donor	nitric oxide concn (mM)	k_{obs} (10^6 s^{-1})	aromatic donor	nitric oxide concn (mM)	k_{obs} (10^6 s^{-1})
HMB	0.14	0.87	DUR	0.11	0.45
	0.34	2.3		0.13	0.54
	0.85	4.8		0.26	1.0
	2.1	9.3		0.53	2.3
PMB	0.10	0.9		0.67	2.8
	0.15	1.3	XYL	0.26	2.5
	0.56	4.2		0.33	3.3
	0.98	7.6		0.48	4.2
	2.2	16		0.55	5.0
				1.1	10.3

[a] By 532-nm excitation with 10-ns (fwhm) laser pulse of solutions containing 10^{-3} M $NO^+BF_4^-$ and 5 mM aromatic donors in nitromethane at 25 °C.

Since the magnitude of the first-order rate constants k_{obs} for the disappearance of $HMB^{\bullet+}$ coincided with that for the first-order return of the CT bleach, we conclude that the spectral change in Figure 3 represented the relaxation of the aromatic cation radical back to the original [Ar,NO^+] complex. Furthermore the parallel increases of the experimental first-order rate constants of k_{obs} with NO concentration, as listed in Table IV, indicated that all of these spectral decays were related to the second-order kinetics for electron transfer, i.e.

$$Ar^{\bullet+} + NO \rightarrow [Ar,NO^+] \qquad (10)$$

Moreover the pseudo-first-order behavior of the spectral decay also applied to other cation radicals such as $DUR^{\bullet+}$ and $XYL^{\bullet+}$, as illustrated in Figure 4 by the linear dependence of k_{obs} with NO concentration following the charge-transfer excitation of the durene and *p*-xylene EDA complexes, respectively. The pseudo-first-order rate constants for the spectral decays of the aromatic cation radicals in acetonitrile solutions of the hexamethylbenzene, pentamethylbenzene, durene, *p*-xylene, and toluene EDA complexes are listed in Table V, together with some of those measured in dichloromethane. As such, the second-order rate constants (k_{II}) for electron transfer between the different aromatic cation radicals and nitric oxide can be evaluated from the slopes of the NO dependence of k_{obs} (compare Figure 4). The resulting values of the experimental rate constant k_{II} in various solvents are listed in Table VI.[61]

VI. Time-Resolved Picosecond Spectroscopic Studies of [Ar,NO^+] Complexes. Quantum yields of less than unity in Table III for the production of aromatic cation radicals suggested the prior participation of some other rapid electron-transfer process(es) that occurred within the earliest stages of the observable time span

(59) Hurley, J. K.; Sinai, N.; Linschitz, H. *Photochem. Photobiol.* **1983**, *38*, 9.

(60) Reddi, E.; Jori, G.; Rodgers, M. A. J.; Spikes, J. D. *Photochem. Photobiol.* **1983**, *38*, 639.

(61) Since a close inspection of the data in Tables IV and V shows a slight trend in the magnitudes of $k_{obs}[NO]^{-1}$ (especially for $HMB^{\bullet+}$ and $PMB^{\bullet+}$), k_{II} in Table VI were evaluated at [NO] = 0. For the origin of the curvature, see the Discussion.

Table V. Solvent Dependence of the Pseudo-First-Order Decays of Aromatic Cation Radicals[a]

aromatic donor	nitric oxide concn (mM)	k_{obs} (10^6 s^{-1})	aromatic donor	nitric oxide concn (mM)	k_{obs} (10^6 s^{-1})
		Acetonitrile			
HMB	0.17	0.70	DUR	0.84	1.6
	0.20	0.73		1.1	2.0
	0.34	1.1		1.1	2.1
	0.49	1.6		1.7	2.8
	0.92	2.3		3.0	5.3
	1.1	2.6		3.5	5.8
	1.8	3.8		4.0	6.2
	2.4	5.4		5.9	9.6
	3.5	6.1		8.0	11
	3.9	6.9	XYL	0.35	0.40
PMB	0.34	0.90		0.80	1.2
	0.52	1.4		0.87	1.2
	0.90	2.5		1.2	1.5
	1.5	4.5		2.3	3.3
	2.4	6.4		4.5	10
	6.0	13	TOL	0.5	1.0
DUR	0.15	0.20		0.75	1.9
	0.22	0.25		0.84	2.0
	0.35	0.50		1.4	2.5
	0.39	0.61		1.8	4.4
	0.63	1.2		2.2	4.7
	0.71	1.4		3.3	8.5
		Dichloromethane[b]			
HMB	0.13	0.65	PMB	1.3	3.9
	0.2	0.8		2.2	6.1
	0.28	1.3	DUR	0.18	0.64
	0.45	2.0		0.24	0.85
	0.78	2.9		0.32	1.2
	2.0	5.8		0.48	1.8
PMB	0.10	0.63		0.70	2.4
	0.20	1.0		1.3	3.8
	0.37	1.5		1.5	4.6
	0.72	2.5			

[a] By 355-nm excitation with 10-ns (fwhm) laser pulse of solutions containing 5–50 mM arene and 1–5 mM $NO^+BF_4^-$ in either acetonitrile or dichloromethane at 25 °C. [b] Containing 10% of CH_3CN for solubility.

Table VI. Experimental Second-Order Rate Constants for Electron Transfer between Aromatic Cation Radicals and Nitric Oxide[a]

aromatic cation radical	solvent	k_{11}[b] (10^9 M^{-1} s^{-1})
$HMB^{\bullet+}$	CH_3NO_2	6.0 ± 0.5[d]
	CH_3CN	2.5 ± 0.5[c,d]
	CH_2Cl_2	4.3 ± 0.5
$PMB^{\bullet+}$	CH_3NO_2	7.7 ± 0.5
	CH_3CN	2.6 ± 0.2
	CH_2Cl_2	4.0 ± 0.5
$DUR^{\bullet+}$	CH_3NO_2	4.5 ± 0.5
	CH_3CN	1.6 ± 0.6
	CH_2Cl_2	3.7 ± 0.2
$XYL^{\bullet+}$	CH_3NO_2	9.3 ± 0.2
	CH_3CN	1.4 ± 0.1
$TOL^{\bullet+}$	CH_3CN	2.3 ± 0.1

[a] At 25 °C. [b] Average of $k_{obs}/[NO]$ up to $[NO] = 5 \times 10^{-4}$ M. [c] $[NO] = 9.2 \times 10^{-4}$ M. [d] Slightly curved plot of k_{obs} versus [NO].

following the CT excitation of the aromatic EDA complexes with the 10-ns laser pulse. Indeed such an extra feature of the kinetics could be observed directly in the time-resolved nanosecond spectra under special circumstances, such as that illustrated in Figure 5 for the temporal decay of the spectral transient of $HMB^{\bullet+}$ generated in nitromethane.[62] Figure 5 shows that the principal, slow component, as reported in Table IV (see inset), was clearly preceded by a rapid dropoff of a minor component with a half-life of ~10 ns. Since the latter lay within the pulse width of the Q-switched laser, we scrutinized the initial component of the biphasic decay by the application of a 20-ps pulse consisting of

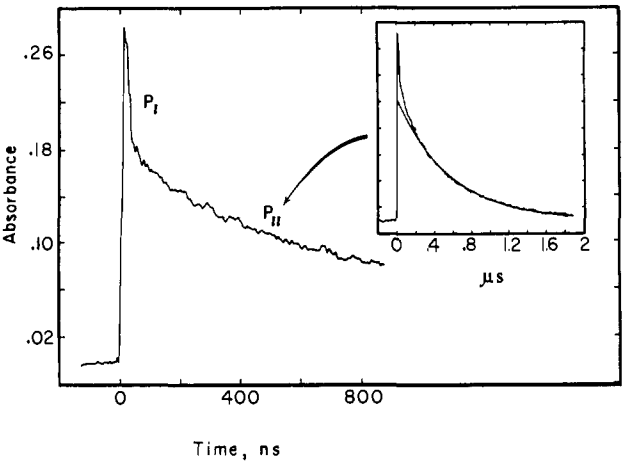

Figure 5. Bimodal spectral decay of $HMB^{\bullet+}$, monitored at λ_{max} = 490 nm following the excitation at 532 nm of the nitromethane solution of 2 mM HMB, 0.8 mM $NO^+BF_4^-$, and 0.3 mM nitric oxide at 25 °C with the 10-ns laser pulse. The inset shows the fit (smooth line) for the pseudo-first-order spectral decay of the slow component on the longer (2 μs) time scale.

the third harmonic at 355 nm of the mode-locked Nd^{3+}:YAG laser corresponding to the excitation of the [Ar,NO^+] complexes at the absorption maxima (or near maxima) of the first high-energy CT absorption bands $h\nu_{CT}$(A) in Table I. Accordingly, the time-resolved spectrum shown in Figure 6A from Ar = hexamethylbenzene (HMB) related directly to the reactive intermediate from the CT excited state of the [HMB,NO^+] complex in acetonitrile. As such there was no ambiguity about either the local excitation[12,13] of complexed (or uncomplexed) chromophores or the photogeneration of intermediates that did not arise from the photoexcitation of the charge-transfer complex (compare Figure 1A). Initially, the intense absorption observed immediately following the 20-ps (fwhm) laser flash consisted of a broad, nonGaussian band in the region 400/500 nm. With time, this nondescript band underwent a segmental transformation (by the preferential decay of the high-energy end) to finally evolve (at 4.5 ns following the laser flash) into the characteristic absorption spectrum of $HMB^{\bullet+}$ by spectral comparison with that shown in Figure 2 and with that spectroelectrochemically generated earlier.[43,63] A similar transformation of the spectral transient occurred in the less polar nitromethane solution but at a slower rate, as shown in Figure 6B by the comparison of the initial picosecond spectra to that of $HMB^{\bullet+}$ (inset) obtained in the microsecond time-interval that is relevant to the results in Table IV. A similar but more subtle spectral change was noted for the spectral transients from the durene EDA complex that showed a measurable shift of the overall band position from λ_{max} = 440 nm at 0 ps to the well-resolved spectrum of $DUR^{\bullet+}$ with λ_{max} = 460 nm[64] at 3.5 ns. In all cases, the changes in the spectral form which consisted of broad bands at early times to the Gaussian bands characteristic of the aromatic cation radicals (observed on the nanosecond time scale) were well correlated to the decay rates. For example, the severely broadened band of the transient absorption derived from the pentamethylbenzene EDA complex at 60 ps in Figure 6C lay at the earliest point among the steep part of the picosecond/nanosecond decay profile (see inset). By contrast, the Gaussian absorption band of $PMB^{\bullet+}$ (λ_{max} = 485 nm)[65] that was taken at 3.5 ns following the laser flash coincided with the latest point after the decay profile had reached a constant, equilibrated value. The comparatively long times at which the spectral differences were observed ruled out the possibility of an instrumental artifact caused by temporal dispersion (chirp) associated with the group velocities of the various probing wave-

(62) Acetonitrile cannot be reliably prepared without traces of water.

(63) See also: Peacock, N. J.; Schuster, G. B. *J. Am. Chem. Soc.* **1983**, *105*, 3632.
(64) See Sehested, Holcman, and Hart in ref 45.
(65) See Dunbar et al. in ref 44 and Hart et al. in ref 45.

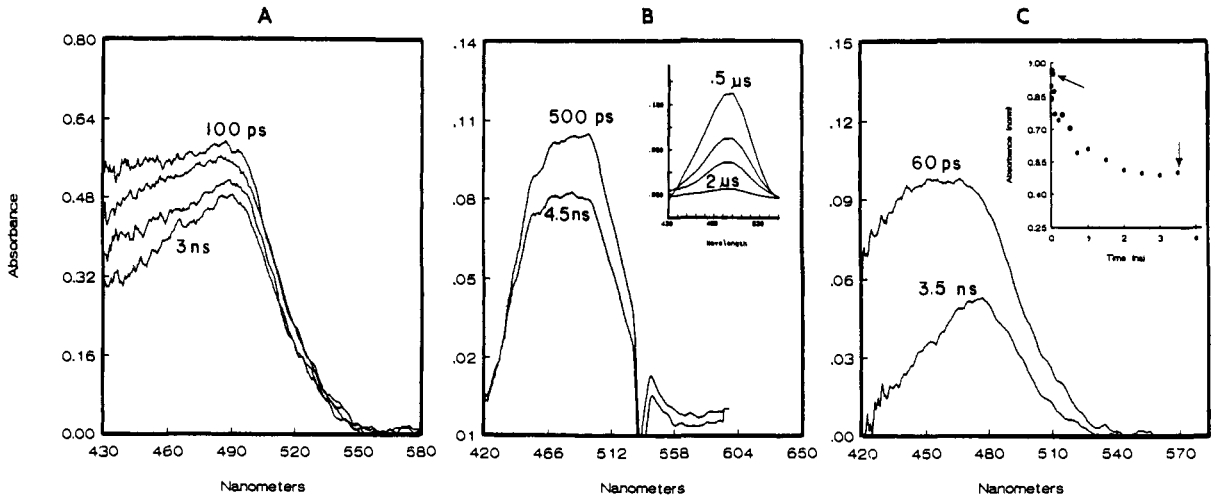

Figure 6. Time-resolved picosecond absorption spectra observed upon the CT excitation of aromatic EDA complexes: (A) [HMB,NO^+] in CH_3CN at 355 nm acquired 0.1, 0.5, 1.0, and 3.0 ns after the laser pulse; (B) [HMB,NO^+] in CH_3NO_2 at 0.5 and 4.5 ns after the pulse with the inset showing the decay of $HMB^{\bullet+}$ in the time interval of 0.5–2.0 μs; (C) [PMB,NO^+] in CH_3CN at 0.06 and 3.5 ns after the pulse. The inset shows the decay of the 480-nm absorbance with the arrows identifying the times of the spectral acquisitions.

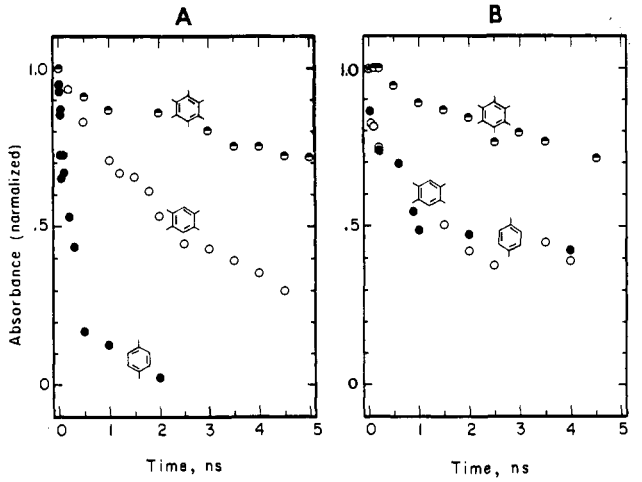

Figure 7. Decay profiles of the absorbances of $HMB^{\bullet+}$ (●), $DUR^{\bullet+}$ (○), and $XYL^{\bullet+}$ (◉) following the 20-ps excitation of the aromatic EDA complexes in nitromethane (A) at 532 nm and in acetonitrile (B) at 355 nm.

lengths. This conclusion was confirmed by the characteristic absorption spectrum that we obtained for the triplet chloranil[66] at times >50 ps by 355-nm excitation at comparable laser power (2 mJ per pulse) and ground-state absorbance ($A \sim 1.5$).

VII. Spectral Decays of the Short-Lived Aromatic Cation Radicals in Solution. Since the spectral transients arising from the 20-ps laser pulse in Figure 6 were responsible for the initial short-lived component of the biphasic decay (see Figure 5), their absorbance changes at λ_{max} were continuously monitored out to beyond 4.5 ns in a pair of solvents of different polarity. In nitromethane, the strong dependence of the decay profile (Figure 7A) on the aromatic donor is shown in two ways. First, the apparent half-life (τ) for the spectral decay of the transient markedly decreased in the following order:[67] $HMB^{\bullet+}$ (τ 2.3 ns) > $DUR^{\bullet+}$ (τ 1.2 ns) > $XYL^{\bullet+}$ (τ 0.16 ns). Second, the residual absorbance (R) after 4.5 ns increased in the same order: $HMB^{\bullet+}$ ($R = 0.70$) > $DUR^{\bullet+}$ ($R = 0.35$) > XYL ($R \sim 0.1$). On the other hand, in the more polar solvent acetonitrile the differentiation of the donors in the decay profiles (Figure 7B) was less marked—with respect to both the apparent halflife [$HMB^{\bullet+}$ (τ 2.1 ns) > $DUR^{\bullet+}$ (τ 0.6 ns) ≈ $XYL^{\bullet+}$ (τ 0.3 ns)] and the residual absorbance [$HMB^{\bullet+}$ ($R = 0.75$) > $DUR^{\bullet+}$ ($R = 0.40$) ≈ $XYL^{\bullet+}$ ($R = 0.40$)]. Since the spectral profiles in Figure 7 represent exponential decays, they are designated hereafter by the experimental first-order rate constant k_1.

VIII. Formation of π-Dimers of Aromatic Cation Radicals at High Donor Concentrations. Since the excitation of [Ar,NO^+] complexes with the 10-ns laser pulse led to the efficient generation of various aromatic cation radicals, we also examined the effect of donor concentration on the spectral transients. For example, the 355-nm excitation of a 7.5 mM solution of benzene and excess (50 mM) $NO^+BF_4^-$ in acetonitrile afforded the transient absorption spectrum in Figure 8A with a prominent band at λ_{max} = 430 nm which was diagnostic of the benzene cation radical (vide supra). When the concentration of benzene was increased to 70 mM (at the same NO^+ concentration), the transient spectrum in Figure 8B showed an additional strong, broad band centered at ~900 nm. The latter was clearly the dominant feature of the transient spectrum in Figure 8C obtained from the CT excitation of a 50 mM solution of $NO^+BF_4^-$ and a very large excess (3.74 M) of benzene. Further increments of benzene had minimal effects on the transient spectrum which was assigned to the π-dimer of the benzene cation radical.[68,69]

In a similar vein, the CT excitation of a solution of 16 mM toluene and 50 mM $NO^+BF_4^-$ in acetonitrile led to a transient spectrum showing a single band at λ_{max} = 430 nm of the monomeric toluene cation radical.[70] The latter was the minor feature of the transient spectrum obtained by increasing the toluene concentration to 0.2 M, being replaced by a dominant broad band centered at ~980 nm of the π-dimer. The cation radical of *o*-xylene was similarly observed at λ_{max} = 435 nm and replaced by the dominant, broad absorption of its π-dimer with λ_{max} > 1050 nm.[70] By comparison, the transient spectra obtained from *tert*-butylbenzene and iodobenzene were unaffected by concentration changes, the monomeric cation radicals with λ_{max} = 470 and 680 nm, respectively, being observed even at high (>1.0 M) donor concentrations with no near-IR bands evident.

(66) (a) Gschwind, R.; Haselbach, E. *Helv. Chim. Acta* **1979**, *62*, 941. (b) Levin, P. P.; Pluzhnikov, P. F.; Kuzmin, V. A. *Chem. Phys. Lett.* **1988**, *147*, 283.

(67) These values of τ were evaluated from the experimental decay profiles that were taken as a single exponential, i.e., $k_1 = (\ln 2)/\tau$. For the complete kinetics treatment, see the Discussion.

(68) Badger, B.; Brocklehurst, B. *Trans. Faraday Soc.* **1969**, *65*, 2576, 2582, 2588.

(69) Shida, T.; Hamill, W. H. *J. Chem. Phys.* **1966**, *44*, 2375.

(70) Badger, B.; Brocklehurst, B.; Russell, R. D. *Chem. Phys. Lett.* **1967**, *1*, 122. See also refs 45, 51, and 68. For other examples, see; (a) Shida, T.; Iwata, S. *J. Am. Chem. Soc.* **1973**, *95*, 3473. (b) Kira, A.; Arai, S.; Imamura, M. *J. Phys. Chem.* **1972**, *76*, 1119; **1971**, *54*, 4890. For ESR studies of the sandwich structures of π-dimers, see: (c) Edlund, O.; Kinell, P.-O.; Lund, A.; Shimizu, A. *J. Chem. Phys.* **1969**, *46*, 3679. (d) Lewis, I. C.; Singer, L. S. *J. Chem. Phys.* **1965**, *43*, 2712. (e) Howarth, O. W.; Fraenkel, G. K. *J. Am. Chem. Soc.* **1966**, *88*, 4514.

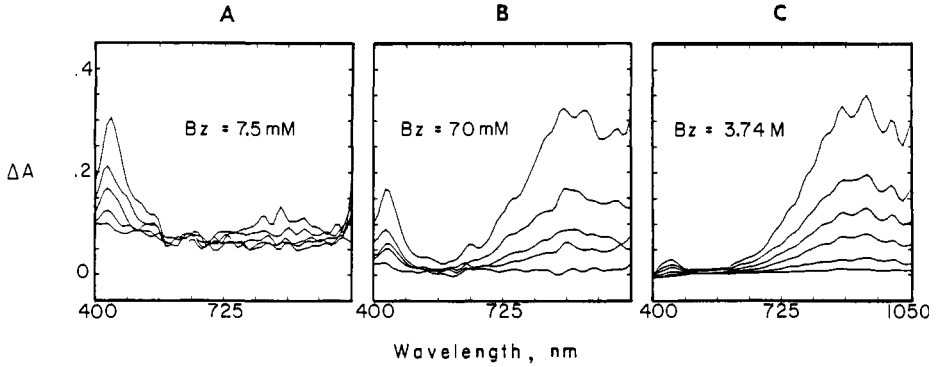

Figure 8. Concentration-dependent evolution of the monomeric benzene cation radical ($BZ^{\bullet+}$, λ_{max} = 430 nm) to the π-dimer ($BZ_2^{\bullet+}$, $\lambda_{max} \simeq$ 900 nm) in acetonitrile containing (A) 7.5 mM, (B) 70 mM, and (C) 3.74 M benzene and 50 mM $NO^+BF_4^-$ (at, from top-to-bottom, 0.2, 0.4, 0.5, 0.7, and 1.0 μs) following the application of the 10-ns laser pulse at 355 nm.

Discussion

The 1:1 molecule–ion complexes of various aromatic donors with the nitrosonium cation are characterized by a pair of charge-transfer absorption bands (designated as A and B in Table I) that are readily observable in the UV–vis spectrum taken in solution (absorption) and in the crystalline solid state (diffuse reflectance). The specific irradiation with a 10-ns (fwhm) laser pulse at 355 or 532 nm of the [Ar,NO^+] complex in acetonitrile solution leads to the bleaching of the CT absorption band and the simultaneous appearance of spectral transients (Figure 2 and Table II) that are identified as aromatic cation radicals ($Ar^{\bullet+}$) by spectral comparison with species independently generated with the aid of transient electrochemical methods or γ-radiolysis and pulse radiolysis.[45-50] The spectral transformations in this manner relate to the charge-transfer excitation ($h\nu_{CT}$) of the [Ar,NO^+] complex to the ion–radical pair state [$Ar^{\bullet+}$,NO][71] according to the Mulliken formulation.[12,13]

I. Dynamics of Transient Ion Radical Pairs. The subsequent decay of the spectral transient by the return of the absorbance to the baseline occurs at the same rate as that for the spectral recovery of the charge-transfer band to confirm the complete regeneration of the aromatic EDA complex with nitrosonium. Such a reversible cycle depends on the efficient back-electron transfer (k_1) between the aromatic cation radical and nitric oxide. The stoichiometry of the overall process is thus consistent with a photostationary state such as

Scheme I

$$[Ar,NO^+] \underset{k_1}{\overset{h\nu_{CT}}{\rightleftharpoons}} [Ar^{\bullet+},NO] \qquad (11)$$

originally envisioned by Mulliken[13] and experimentally observed with some other electron acceptors.[72] For the NO^+ acceptor studied here, however, the more detailed kinetics examination of the spectral decay of $Ar^{\bullet+}$ reveals a biphasic behavior (labeled P_I and P_{II} in Figure 5) with strongly differentiated relaxation times for short-lived and long-lived aromatic cation radicals, respectively. The initial portion of the decay profile (P_I) is completed within the time interval of a few nanoseconds following the application of the laser pulse, whereas the later, slow decay (P_{II}) is observed in the time span of up to several microseconds (Figure 3). Such a sharp delineation of the spectral decay into two distinct stages (differentiated by a 10^3 factor) allows the kinetics analysis to be largely dissected into separate phases. Accordingly, the two different pulsed-laser systems are used to examine the relaxation of [$Ar^{\bullet+}$,NO] over two discrete time domains—ps/ns and ns/μs for P_I and P_{II} of the ion radical pair dynamics, as follows.

II. Picosecond Dynamics of Ion Radical Pairs Leading to Inner-Sphere Electron Transfer and Diffusive Separation. The time-resolved picosecond spectroscopy leads to the three characteristic profiles shown in Figure 7A for the transient decay (k_1) of the aromatic cation radicals $HMB^{\bullet+}$, $DUR^{\bullet+}$, and $XYL^{\bullet+}$ following the 20-ps laser pulse excitation of the hexamethylbenzene, durene, and *p*-xylene EDA complexes with nitrosonium. At one kinetic extreme, the $XYL^{\bullet+}$ absorbance decays rapidly to the baseline and only a small residual (R) is apparent beyond 1 ns. At the other extreme, the $HMB^{\bullet+}$ absorbance remains largely intact within the same period. Finally the decay of $DUR^{\bullet+}$ shows intermediate behavior—leveling off to a limiting absorbance that is roughly 30% of the initial value. Since the stoichiometry demands the ultimate return of the aromatic cation radical to the original EDA complex (vide supra), Scheme I must be modified to account for the $Ar^{\bullet+}$ fraction that is unavailable for back-electron transfer (k_1) in this time interval—most reasonably by diffusive separation (k_s), i.e.

Scheme II

$$[Ar^{\bullet+},NO] \xrightarrow{k_s} Ar^{\bullet+} + NO \qquad (12)$$
$$\downarrow k_1$$
$$[Ar,NO^+]$$

According to the mechanism in Scheme II, the transient absorbance A_t at a given time t represents the composite contributions of both [$Ar^{\bullet+}$,NO] and $Ar^{\bullet+}$, i.e.[73]

$$A_t = \exp[-(k_1 + k_s)t] + k_s(k_1 + k_s)^{-1}\{1 - \exp[-(k_1 + k_s)t]\} \qquad (13)$$

$$= \frac{k_s}{k_1 + k_s} + \frac{k_1}{k_1 + k_s}\exp[-(k_1 + k_s)t] \qquad (14)$$

Since the ratio of rate constants represents the residual of the absorbance (R), it is obtained directly from the quantum yield Φ evaluated in Table III, i.e.

$$\Phi = k_s/(k_1 + k_s) \qquad (15)$$

Accordingly, the time-dependent absorbance in eq 14 can be reexpressed as

$$A_t = \Phi + (1 - \Phi)\exp[-(k_1 + k_s)t] \qquad (16)$$

The analytical solution of eq 16 (see Experimental Section) yields the values of the composite rate constants $(k_1 + k_s) = k_1$ listed in Table VII, column 3, for the various aromatic cation radical pairs in two solvents of different polarity.[74] The graphical fit of the calculated decay (smooth curve in Figure 9) based on eq 16 to the experimental points provides strong support for the

(71) The term *ion radical pair* is used to describe [Ar^+,NO], consonant with the description of the (transient) *ion pairs* formed upon charge-transfer excitation of other EDA complexes, as presented in ref 72.

(72) See for example: Takahashi, Y.; Sankararaman, S.; Kochi, J. K. *J. Am. Chem. Soc.* **1989**, *111*, 2954. Wallis, J. M.; Kochi, J. K. *J. Am. Chem. Soc.* **1988**, *110*, 8207.

(73) Yabe, T.; Sankararaman, S.; Kochi, J. K. *J. Phys. Chem.* **1991**, *95*, 4177. Equation 16 is based on negligible reassociation (see Scheme III), i.e., $k_a[NO] \ll (k_1 + k_s)$, see Appendix.

(74) Reichardt, C. *Solvent Effects in Organic Chemistry*; Verlag Chemie: New York, 1979.

Table VII. Picosecond Dynamics of the Aromatic Cation Radical Pairs

$[Ar^{\bullet+}NO]^a$ ($Ar^{\bullet+}$)	solvent	$(k_1 + k_s)^b$ (10^8 s^{-1})	$k_1{}^c$ (10^8 s^{-1})	$k_s{}^c$ (10^8 s^{-1})
$HMB^{\bullet+}$	CH_3CN	3.3 (3.3)	1.0 (1.0) ± 0.1	2.3 (2.3) ± 0.2
	CH_3NO_2	3.0 (2.5)	0.9 (0.8) ± 0.1	2.1 (1.8) ± 0.2
$PMB^{\bullet+}$	CH_3CN	10 (10)	4.0 (4.0) ± 0.5	6.0 (6.0) ± 0.5
$DUR^{\bullet+}$	CH_3CN	12 (13)	7 (7) ± 2	5 (6) ± 2
	CH_3NO_2	6 (4.8)	4.0 (3.6) ± 0.2	~2 (1.2) ± 0.2
$XYL^{\bullet+}$	CH_3CN	22 (25)	13 (14) ± 3	9.0 (11) ± 3
	CH_3NO_2	44 (40)	37 (35) ± 5	7 (4) ± 0.5
$TOL^{\bullet+}$	CH_3CN	(200)[d]	(200) ± 100	(~11)[e]

[a] Generated by 20-ps excitation at 355-nm (CH_3CN) or 532-nm (CH_3NO_2) of [Ar,NO⁺] from 4 mM Ar and 2 mM $NO^+BF_4^-$ containing <0.1 mM NO. [b] Obtained from the experimental rate constant k_1 in Figure 7 and from the values of Φ in Table III. [c] Evaluated from column 3 and eq 15. The values in parentheses calculated from the graphical fit (see Experimental Section). [d] See Experimental Section. [e] Assumed to be the same as k_s for ($XYL^{\bullet+}$).

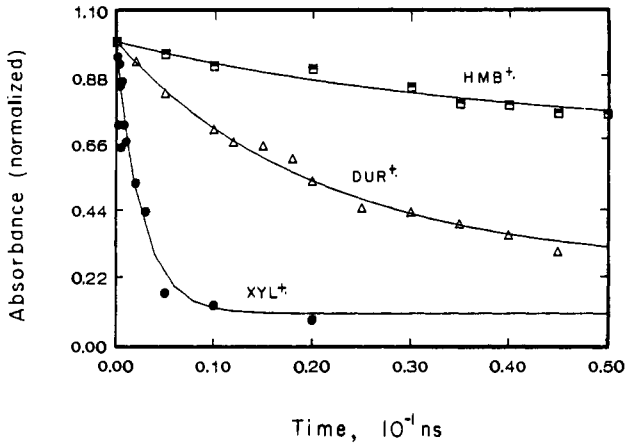

Figure 9. Graphical fit of the calculated (picosecond) decay (smooth curve) based on eq 16 to the experimental points from $HMB^{\bullet+}$ (■), $DUR^{\bullet+}$ (△), and $XYL^{\bullet+}$ (●) in Figure 7A.

kinetics formulation in Scheme II.

The basic mechanism as outlined in Scheme II bears a direct resemblance to another general problem involving the kinetics behavior of geminate free radical pairs[75]—involving as it does the direct competition between cage collapse (k_1) and diffusive separation (k_s). It is thus instructive to compare the values of k_s listed in Table VII with those involving the diffusive separation of uncharged radicals with $k_s \sim 10^9$ s^{-1}.[76] Although the rates of diffusive separation of [$TOL^{\bullet+}$,NO] and [$XYL^{\bullet+}$,NO] generally accord with the behavior of geminate free radicals, the value of $k_s = 2 \times 10^8$ s^{-1} for [$HMB^{\bullet+}$,NO] appears to be unaccountably slower.[77] In order to examine this apparent anomaly, let us consider the microscopic reverse involving the rates of (re)*association* of the free species $Ar^{\bullet+}$ and NO that is allowed by the kinetics analysis of the microsecond data. Before doing so, however, it is important to note that the magnitudes of k_1 (Table VII, column 4), which we define as the first-order rate constant for *inner-sphere* electron transfer, vary by only a factor of ~10^2 between $HMB^{\bullet+}$ and $TOL^{\bullet+}$, despite a difference in driving force of more than 0.8 eV or ~20 kcal mol^{-1}.

III. Direct Observation of the Cation Radical Pair [$Ar^{\bullet+}$,NO^-] in the Picosecond Spectra. The careful scrutiny of the time-resolved picosecond spectra (Figure 6) reveals the spectral transient responsible for P_I to consist of (at least) two closely related components—the more persistent transient observed at the longest time delays (4.5 ns) being unambiguously identified as the aromatic cation radical ($Ar^{\bullet+}$). The other component is characterized by a slight spectral shift, and it is only observed at the *earliest* times following the 20-ps laser pulse. The difference points to a perturbation of the electronic energy levels of the aromatic cation radical, and it is reminiscent of that previously ascribed to the local bands of an electron acceptor upon its complexation with various donors.[78] Accordingly, we assign the second, highly labile component of the spectral (ps) transient to the initial ion radical pair [$Ar^{\bullet+}$,NO], as indeed predicted by Mulliken's theory of charge transfer.[13] The temporal evolution of the time-resolved picosecond spectra in Figure 6 thus provides independent support of the ion radical separation (k_s), as presented in Scheme II.

Table VIII. Second-Order Rates and Equilibria for the (Re)association of $Ar^{\bullet+}$ and Nitric Oxide

$Ar^{\bullet+}$	solvent	$k_a{}^a$ (10^9 M^{-1} s^{-1})	$k_2^{IS}{}^b$ (10^9 M^{-1} s^{-1})	K_A (M^{-1})
$HMB^{\bullet+}$	CH_3CN	7 ± 2	2.1	30
	CH_3NO_2	17 ± 3	5.4	94
$PMB^{\bullet+}$	CH_3CN	7 ± 1	2.6	11
$DUR^{\bullet+}$	CH_3CN	3.0 ± 0.6	1.6	5.0
	CH_3NO_2	6.0 ± 0.7	4.5	50
$XYL^{\bullet+}$	CH_3CN	2.5 ± 0.2	1.4	2.3
	CH_3NO_2	11 ± 1	9.2	27
$TOL^{\bullet+}$	CH_3CN	<2	2.3	~2

[a] From eq 19 and k_1 and k_s from Table VII. [b] From eq 25, see Experimental Section.

IV. Microsecond Dynamics for the (Re)association of the Separated $Ar^{\bullet+}$ and Nitric Oxide. The NO dependence of the spectral decay, as reported in Tables IV and V, relates directly to the second-order kinetics for the annihilation of $Ar^{\bullet+}$ and NO. Such a process modifies the ion radical dynamics in Scheme II by taking into consideration the diffusive (re)association (k_a) of $Ar^{\bullet+}$ and nitric oxide, i.e.

Scheme III

$$[Ar^{\bullet+},NO^-] \underset{k_a}{\overset{k_s}{\rightleftharpoons}} Ar^{\bullet+} + NO \qquad (17)$$

$$[Ar^{\bullet+},NO^-] \xrightarrow{k_1} [Ar,NO^+]$$

The complete rate expression for the mechanism in Scheme III is given by the double exponential

$$A_t = C_1 e^{-\lambda_1 t} + C_2 e^{-\lambda_2 t} \qquad (18)$$

where the composite rate constants λ_1 and λ_2 together with the constants C_1 and C_2 are described in the Appendix. Equation 18 thus describes the successive decays I and II that are experimentally observed and depicted by Figure 5, in which λ_1 and λ_2 are the determinants for P_I and P_{II}, respectively. Owing to the complete separation of these time domains, the slower spectral decay associated with P_{II} is readily evaluated by the expression

$$\ln A_t/t = -0.5\{\kappa - (\kappa^2 - 4k_1k_a[NO])^{1/2}\} \qquad (19)$$

where $\kappa = k_1 + k_s + k_a[NO]$ as derived in the Appendix. The

(75) (a) Noyes, R. M. *Prog. React. Kinet.* **1961**, *1*, 129. (b) Calef, D. F.; Deutch, J. M. *Annu. Rev. Phys. Chem.* **1983**, *34*, 493. See also: Koenig, T.; Fischer, H. In *Free Radicals*; Kochi, J. K., Ed.; Wiley: New York, 1973; Vol. 1, p 157 ff.

(76) Noyes, R. M. *J. Chem. Phys.* **1954**, *22*, 1349.

(77) Diffusion coefficient of $HMB^{\bullet+}$ is not significantly different from that of either $TOL^{\bullet+}$ or $XYL^{\bullet+}$.

(78) Such a spectral shift is observed in aromatic EDA complexes of iodine, as shown in Figure 1 of ref 37.[13]

Table IX. Rate and Equilibrium Constants for Outer-Sphere and Inner-Sphere Electron Transfer According to Scheme IV

aromatic donor	K_{EDA}[a] (M^{-1})	$-\Delta G_{OS}$[b] (kcal mol^{-1})	K_{OS}[c]	k_2[d] (M^{-1} s^{-1})	k_{-2}[e] (M^{-1} s^{-1})	K_A[f] (M^{-1})	$-\Delta G_{IS}$[c] (kcal mol^{-1})	K_{IS}[g]	k_1[h] (s^{-1})	k_{-1}[i] (s^{-1})
HMB	3.1×10^4	7.8	5.6×10^5	1.9×10^6	4.0	30	12.0	6.3×10^8	1×10^8	0.16
PMB	5.0×10^3	10.4	4.1×10^7	1.0×10^7	0.24	11	14.1	2.1×10^{10}	4×10^8	0.20
DUR	4.5×10^2	11.8	4.2×10^8	2.4×10^7	0.057	5	14.5	4.5×10^{10}	7×10^8	0.015
XYL	3.0×10	17.1	3.3×10^{12}	4.1×10^8	1.2×10^{-4}	2.3	18.7	5.0×10^{13}	1×10^9	2.8×10^{-5}
TOL	5	25.8	8.8×10^{18}	1.2×10^{10}	1.4×10^{-9}	2.2	26.3	1.9×10^{19}	2×10^{10}	1.0×10^{-9}

[a] In acetonitrile at 25 °C from ref 19. [b] From E_{Ar} and E_{NO^+} in refs 33 and 6. [c] See text. [d] From Marcus eq 23. [e] From K_{OS} and k_2. [f] From Table VIII. [g] From Scheme IV with K_{EDA}, K_{OS}, and K_A. [h] From Table VII. [i] From K_{IS} and k_1.

graphical fit of the experimental rate constants, $k_{obs}t = \ln A_t$, to the rate data in Tables IV and V with the aid of the values of k_1 and k_s in Table VII yielded the (re)association constants k_a and $k'_2 = k_{obs}[NO]^{-1}$ presented in Table VIII (see Experimental Section for details). The values of the equilibrium constants for (re)association, $K_A = k_a/k_s$, evaluated from the results in Table VIII (column 3) and Table VII (column 5), i.e.

$$Ar^{\bullet+} + NO \overset{K_A}{\rightleftharpoons} [Ar^{\bullet+},NO] \qquad (20)$$

are listed in column 5 of Table VIII. Two trends are readily discerned. First, the (re)association constant (K_A) is dependent on solvent polarity, being consistently larger in nitromethane relative to acetonitrile for all the aromatic cation radicals. In particular, the values of $K_A = 94$ and 30 M^{-1} for $HMB^{\bullet+}$ point to the enhanced stabilization of the ion radical pair relative to the freely diffusing species by 2.7 and 2.0 kcal mol^{-1} respectively in nitromethane and acetonitrile. Second, the propensity for (re)association decreases monotonically with the number of methyl substituents on the aromatic cation radical, K_A, decreasing by a factor of ~15 on proceeding from $HMB^{\bullet+}$ to $TOL^{\bullet+}$. Interestingly, this trend parallels the formation constants for the precursor EDA complex, as shown by the comparison of the K_{EDA} values in Table I (column 5). In other words, those factors involved in the ground-state stabilization of the $[Ar,NO^+]$ complex are also pertinent to the stabilization of the ion radical pair $[Ar^{\bullet+},NO]$, but in the diminished degree shown in Figure 10.[79]

For the EDA complexes in general, the binding of the electron donor (D) to the electron acceptor (A) is generally described in valence-bond terms as[13,80]

$$\Psi_{GS} = \frac{1}{N}[a\phi_0 + b\phi_1 + ...] \qquad (21)$$

where the ground-state wave function Ψ_{GS} mainly contains contributions from ϕ_0 and ϕ_1 representing weak van der Waals or the no-bond interaction of D,A and the dative or charge-transfer component D^+A^-, respectively, and N is the normalization factor. The formation constants of such strong EDA complexes as $[Ar,NO^+]$ show a strong dependence on the ionization potential of the aromatic donor (compare columns 2 and 7 in Table I), and the charge-transfer contribution dominates, i.e. $b^2 \gg a^2$.[19] According to Mulliken theory, the imbalance also qualitatively applies to the charge-transfer excited state,

$$\Psi_{ES} = \frac{1}{N}[b\phi_0 - a\phi_1 + ...] \qquad (22)$$

and by association to the ion radical pair $[Ar^{\bullet+},NO]$. In other words, the same charge-transfer forces that are so important to the ground-state stabilization of the $[Ar,NO^+]$ complex can also contribute to the stabilization of the ion radical pair to the reduced degree shown in Figure 10. Furthermore, the existence of such charge-transfer forces accounts for the observed variations in the otherwise anomalous separation rates (k_s) in Table VII and the reverse trend in the (re)association rates (k_a) in Table VIII.

V. Delineation of Outer-Sphere and Inner-Sphere Mechanisms for Electron Transfer. The time-resolved spectroscopic studies

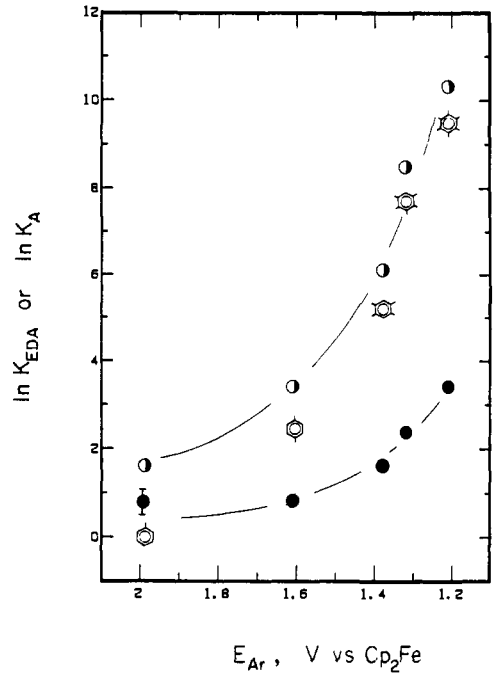

Figure 10. Comparison of the formation constants for the EDA complexes K_{EDA} (◑) and for the cation radical pair K_A (●) with the absolute value of the oxidation potential of the aromatic donors as indicated.[97]

Scheme IV

$$\begin{array}{ccc} [Ar^{\bullet+},NO] & \overset{k_s}{\underset{k_a}{\rightleftharpoons}} & Ar^{\bullet+} + NO \\ k_{-1}\downarrow\uparrow k_1 & & k_{-2}\downarrow\uparrow k_2 \\ [Ar,NO^+] & \overset{K_{EDA}}{\rightleftharpoons} & Ar + NO^+ \end{array}$$

as presented in Scheme III identify two electron-transfer processes for the return of the aromatic cation radical and nitric oxide—namely, that proceeding directly from the geminate pair $[Ar^{\bullet+},NO]$ and that arising via the freely diffusing species $Ar^{\bullet+}$ and NO; and these are associated with the observed first-order (k_1) and second-order (k_{II}) kinetics in Figure 7 and Table VI, respectively. In order to emphasize this kinetics dichotomy, let us extend Scheme III by the inclusion of the ground-state preequilibrium (K_{EDA}) for the formation of the EDA complex, as shown in Scheme IV.

The thermochemical cycle in Scheme IV identifies the rate constants k_1 and k_2 with the *inner-sphere* and *outer-sphere* mechanisms for electron transfer, respectively, of the types often encountered in wholly inorganic redox systems.[81,82]

A. Outer-Sphere Electron Transfer between Aromatic Cation Radicals and Nitric Oxide. Outer-sphere electron transfer as indicated by the rate constant k_2 in Scheme IV also relates to the outer-sphere redox equilibrium with $K_{OS} = k_2/k_{-2}$. As such, the

(79) For example K_{EDA} for $[HMB,NO^+]$ is larger than K_A for $[HMB^{\bullet+},NO]$ by a factor of 10^3.

(80) Hanna, M. W.; Lippert, J. L. *Molecular Complexes*; Foster, R., Ed.; Elek. Science: London, 1973; Vol. 1, p 6 ff.

(81) This mechanistic categorization is based solely on the consideration of the activation process(es). For further implications on the kinetics, see the Discussion.

(82) Compare with the following: Kochi, J. K. *Angew. Chem., Int. Ed. Engl.* **1988**, *27*, 1227.

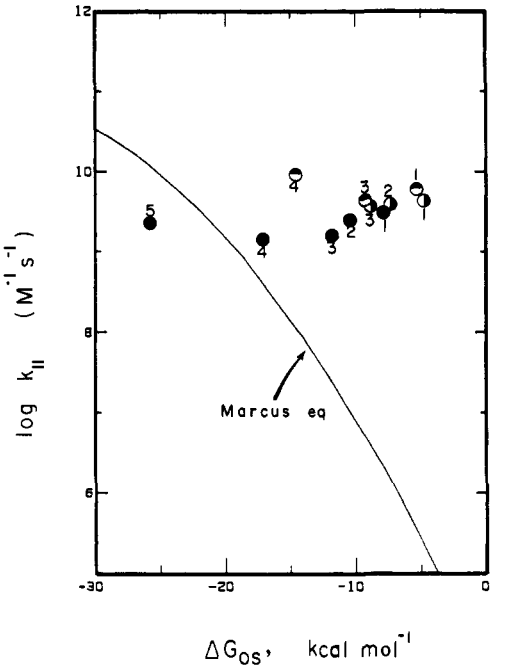

Figure 11. Variation of the experimental second-order rate constants k_{II} for electron transfer of $Ar^{\bullet+}$ with NO with the outer-sphere driving force ΔG_{OS} in CH_3CN (●), CH_3NO_2 (◒), and CH_2Cl_2 (◑) for HMB (1), PMB (2), DUR (3), XYL (4), and TOL (5). The smooth curve is calculated from Marcus eq 23 with λ = 40 kcal mol^{-1}.

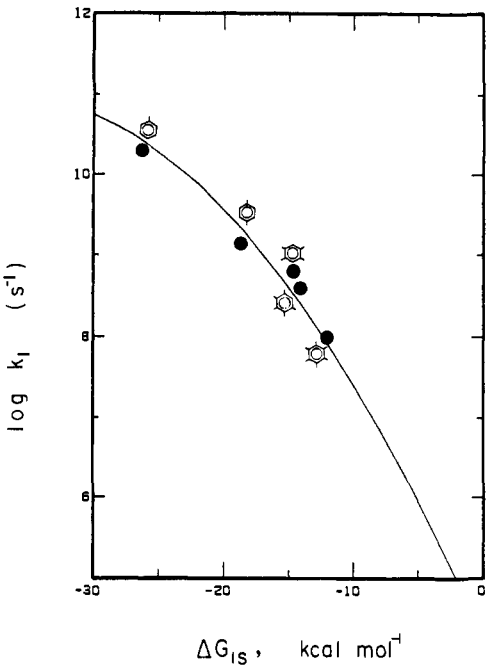

Figure 12. Dependence of the experimental first-order constant k_1 on the inner-sphere driving force ΔG_{IS} for geminate recombination of the cation radical pair $[Ar^{\bullet+},NO]$ in acetonitrile. The smooth curve is calculated from the Marcus equation with λ' = 37 kcal mol^{-1}.

dependence of the electron-transfer rate on the aromatic donor is predicted by the Marcus relationship[83]

$$k_2 = Z \exp\{-\lambda[1 + \Delta G_{OS}/\lambda]^2/4RT\} \quad (23)$$

where the reorganization energy is taken as λ = 40 kcal mol^{-1} [84] and the driving force $-\Delta G_{OS}$ is given by

$$RT \ln K_{OS} = \mathcal{F}(E_{Ar} + E_{NO^{\bullet}}) \quad (24)$$

The values of $-\Delta G_{OS}$ and K_{OS} in Table IX are based on independent measurements of the reversible oxidation and reduction potentials of the aromatic donor E_{Ar} and nitrosonium $E_{NO^{\bullet}}$, respectively, and the Faraday constant $\mathcal{F}$.[85-87]

It is singularly noteworthy that the trend in the experimental values of the second-order rate constant k_{II} evaluated in Table VI bears no relationship (Figure 11) to that of the outer-sphere electron-transfer rates predicted by Marcus theory. More to the point, the experimental k_{II} is essentially invariant with the driving force—both in polar (acetonitrile) and nonpolar (dichloromethane and nitromethane) solvents.[88] Clearly, an alternative mechanism must be considered for the return of $Ar^{\bullet+}$ and NO to the original EDA complex.

B. Inner-Sphere Electron Transfer via the Cation Radical Pair. The outer-sphere electron transfer as given by the rate constant k_2 in Scheme IV represents the direct mechanism for electron transfer.[89] The other, more circuitous, pathway proceeds via the transformation of the (inner-sphere) cation radical pair $[Ar^{\bullet+},NO]$ to the charge-transfer complex $[Ar,NO^+]$. The overall second-order rate constant k_2^{IS} for such an inner-sphere pathway for electron transfer (see k_1 in Scheme IV) can be described in terms of the preequilibrium association (k_a) and separation (k_s) steps as

$$k_2^{IS} = k_1 k_a/(k_1 + k_s) \quad (25)$$

The calculated values of k_2^{IS} based on the steady-state expression in eq 25 are included in Table VIII (column 3). The close correspondence between k_2^{IS} in Table VIII and the experimental rate constant k_{II} in Table VI indeed supports the steady-state formulation, in which the cation radical pair $[Ar^{\bullet+},NO]$ reacts faster than it forms, i.e., $(k_1 + k_s) > k_a[NO]$.[90] If we consider, for the moment, the inner-sphere electron transfer with a rate-limiting k_1 in the context of Marcus eq 23, the driving force $-\Delta G_{IS}$ taken from the thermochemical cycle in Scheme IV is represented as a combination of the outer-sphere contribution ΔG_{OS} and the complexation, i.e., $\Delta G_{IS} = \Delta G_{OS} + \Delta G_{EDA} - \Delta G_A$. The resulting free energy relationship of the electron-transfer rate (log k_1) with the driving force ($-\Delta G_{IS}$) is shown by the smooth curve in Figure 12. The suitable fit of the experimental rate constant (log k_1) to the Marcus curve is based on an optimized reorganization energy of λ' = 37 kcal mol^{-1}.[91] Since this value of the activation barrier is close to the corresponding outer-sphere barrier (vide supra), it suggests that the transition states for the k_1 and k_2 processes bear a strong resemblance to each other.[92,93] In other words, the mechanistic distinction between the inner-sphere and

(83) Marcus, R. A. *J. Chem. Phys.* **1956**, *24*, 966. See also: Marcus, R. A. *Annu. Rev. Phys. Chem.* **1964**, *15*, 155.

(84) (a) Eberson, L.; Radner, F. In ref 4b. (b) The preexponential factor is taken as $Z = 10^{11}$ s^{-1}.

(85) Amatore, C. A.; Kochi, J. K. *Adv. Electron-Transfer Chem.* **1991**, *1*, 53.

(86) (a) Lee, K. Y.; Kuchynka, D. J.; Kochi, J. K. In ref 6. (b) Dean, J. A. *Lange's Handbook of Chemistry*, 13th ed.; McGraw-Hill: New York, 1985.

(87) Correction of the driving force as given in eq 24 by the stability of the EDA complex (i.e. $\Delta G_{EDA} = -RT \ln K_{EDA}$) yields increased outer-sphere rate constants of k_2 = 8.35, 17.5, 17.5, 102, and 1400 × 10^7 M^{-1} s^{-1} by Marcus eq 23.

(88) Although this situation is often encountered in diffusion-controlled reactions, the independent evaluation of the diffusion coefficents (see Experimental Section) indicates k_{II} to be at least an order of magnitude removed from this kinetic limit.

(89) Outer-sphere precursor and successor complexes which may also be involved in such a direct process (see Cannon in ref 31) are considered to be rapid equilibria.[81]

(90) This kinetic situation is valid for all the data in Tables IV and V, except at the highest NO concentrations. Of the various arene donors, it is least applicable to HMB, and the significant deviation from linearity necessitates the application of the exact kinetics expression (eqs 18 and 19) rather than the truncated, simplified form (eq 25) for the data analysis.

(91) The value of λ' = 37 kcal mol^{-1} was obtained by the graphical fit of the Marcus equation to the experimental points by using it as an adjustable parameter.

(92) Hammond, G. S. *J. Am. Chem. Soc.* **1955**, *77*, 334.

(93) Although this conclusion is unlikely to be general, it is probably applicable for this redox system owing to the minimal distortion of $Ar^{\bullet+}$ and the simple diatomic nature of nitric oxide.

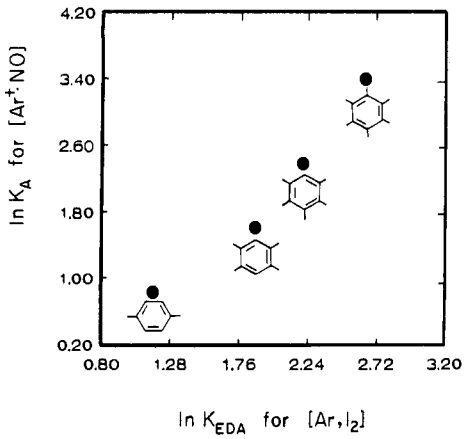

Figure 13. Direct relationship of the formation constants (ln K_{EDA}) of the typical aromatic EDA complexes [Ar,I_2] with the association constants (ln K_A) of the cation radical pair [Ar$^{\bullet+}$,NO].

outer-sphere electron transfer of Ar$^{\bullet+}$ and NO lies in the formation (K_A) of the (inner-sphere) cation radical pair [Ar$^{\bullet+}$,NO] as the kinetically dominant intermediate. In order to emphasize this conclusion, let us rearrange the second-order inner-sphere rate constant in eq 25 to

$$\frac{1}{k_2^{IS}} = \frac{1}{k_a} + \frac{1}{K_A k_1} \qquad (26)$$

Indeed this form of eq 24 identifies the opposing trends of K_A and k_1 (see Tables VIII and VII, respectively) to be responsible for the insensitivity of the second-order rate on the driving force for electron transfer, as illustrated in Figure 11. Therefore we conclude that those factors leading to faster inner-sphere rates (k_1) are offset by the decreased stabilization (K_A) of the precursor, i.e., the inner-sphere cation radical pair. For example, the ~ 15-fold faster inner-sphere rate of XYL$^{\bullet+}$ relative to that of HMB$^{\bullet+}$ (see Table VII) owing to the greater driving force ($-\Delta G_{IS}$ in Table IX) is more or less compensated by the comparable increase in the stabilization of [HMB$^{\bullet+}$,NO] relative to [XYL$^{\bullet+}$,NO] (see Table VIII). Such an important variation in K_A with the aromatic donor results from the association rates (k_a) that decrease, but separation rates (k_s) that increase, on proceeding from HMB$^{\bullet+}$ to XYL$^{\bullet+}$. It is noteworthy that the value of k_a = 1.1 × 10^{10} M^{-1} s^{-1} is close to the encounter-controlled rate constant calculated from the Smoluchowski equation.[94,95] If so, the value of k_a = 1.7 × 10^{10} M^{-1} s^{-1} for HMB$^{\bullet+}$ is faster than can be expected. Conversely, the separation rate constants k_s ~ 10^9–10^8 s^{-1} are at least an order of magnitude slower than that expected from freely diffusing species.[96] Both trends can be rationalized by the intermolecular forces that bind the cation radical pair over relatively long distances of separation. Qualitatively, this may be pictured as a charge-transfer interaction of the aromatic cation radical and nitric oxide. Indeed Figure 13 shows the formation of the cation radical pair [Ar$^{\bullet+}$,NO] to be strongly correlated with that of the well-known aromatic charge-transfer complexes with iodine [Ar,I_2].[97,98]

The importance of (inner-sphere) complexation on electron transfer is also manifested in the inner-sphere redox equilibrium constants $K_{IS} = k_1/k_{-1}$ listed in Table IX which are significantly larger than the corresponding outer-sphere redox constants $K_{OS} = k_2/k_{-2}$, especially for the electron-rich HMB and PMB.[99] The difference is largely associated with the enhanced stabilization of the ground-state complex as shown by the very large formation constants of [HMB,NO$^+$] and [PMB,NO$^+$] in Table I. Thus the enhanced degree of charge transfer in the ground states of these complexes[19] is not directly manifested in the faster rates of inner-sphere electron transfer (k_1).

Conclusions

Photoexcitation of the charge-transfer bands of the aromatic EDA complexes [Ar,NO$^+$] using the 10-ns (fwhm) laser pulse at 355 or 532 nm affords with equally high quantum efficiency the spectral transient that is identified as the aromatic cation radical (Ar$^{\bullet+}$), together with nitric oxide according to eq 9. The temporal relaxation of Ar$^{\bullet+}$ and NO by back-electron transfer to quantitatively regenerate the original EDA occurs in two kinetic phases I and II which are separately measured by time-resolved ps/ns and ns/μs spectroscopy.

Phase I occurs with first-order kinetics (k_1) associated with the collapse of the geminate ion radical pair [Ar$^{\bullet+}$,NO] by an inner-sphere electron transfer to the EDA complex [Ar,NO$^+$]. The relatively slow rates with k_1 ~ 10^8 s^{-1} arise from driving forces $-\Delta G_{IS}$ that approach the isoergonic region, coupled with the rather high reorganization energy of nitric oxide. These allow effective competition from diffusive separation (k_s) to form Ar$^{\bullet+}$ and NO as kinetically separate entities.

Phase II occurs with second-order kinetics (k_{II}) associated with the back-electron transfer from the freely diffusing Ar$^{\bullet+}$ and NO. Comparison of the second-order rate constant k_2 calculated from Marcus theory shows that outer-sphere electron transfer is too slow to account for the experimental values of k_{II}—most notably with HMB$^{\bullet+}$, PMB$^{\bullet+}$, and DUR$^{\bullet+}$ in Figure 11. With the aid of the thermochemical cycle in Scheme IV, the second-order rate is unambiguously identified as the alternative, more circuitous inner-sphere pathway involving the (re)association (k_a) of Ar$^{\bullet+}$ and NO to form the cation radical pair followed by the collapse to [Ar,NO$^+$], as in phase I.

The redox system described in this study has thus presented a unique opportunity to examine the microdynamics for electron transfer with driving forces close to the isoergonic region. In this thermodynamics region, the electron-transfer dynamics are clearly dominated by the inner-sphere complex since all other factors contributing to the intrinsic barrier take on increasing importance (in the absence of the driving force). This situation contrasts with those encountered in most photoinduced redox systems,[20-26] in which the back-electron transfer occurs in the highly exergonic region and the inner-sphere complex is not evident[100] and/or kinetically unimportant. At the other extreme more commonly encountered in organic and organometallic systems, we believe that the inner-sphere pathway will play an important role in the modulation of electron-transfer dynamics, although the complex may be difficult to detect experimentally.[101]

Experimental Section

Materials. Aromatic donors (reagent grade) were purified either by distillation or by recrystallization: benzene, bromobenzene (Mallinck-

(94) Smoluchowski, M. V. *Phys. Z.* **1916**, *17*, 557, 983.

(95) The encounter rate constant k_e was calculated from the diffusion coefficient in Table X and an encounter distance of 3.5 Å[19] as k_e = 1.1, 1.0, and 0.9 × 10^{10} M^{-1} s^{-1} in nitromethane, dichloromethane and acetonitrile, respectively. These calculations do not include any spin restrictions on the encounter rate (compare with the following: Garst, J. F. *J. Chem. Soc., Faraday Trans. 1* **1989**, *85*, 1245).

(96) See: Eberson, L. In ref 20, Table 1, p 34.

(97) As charge-transfer complexes are concerned, the cation-radical pair [Ar$^+$,NO] is unique in that the HOMO-LUMO energy gap is *negative*. Accordingly, we suggest that their comparison with the more usual EDA complexes should be based on the absolute value of the HOMO-LUMO gap, i.e., by the energy displacement away from $E_{HOMO} = E_{LUMO}$.

(98) (a) Andrews, L. J.; Keefer, R. M. *J. Am. Chem. Soc.* **1952**, *74*, 4500. (b) Keefer, R. M.; Andrews, L. J. *J. Am. Chem. Soc.* **1955**, *77*, 2164.

(99) It is interesting to note that the enhanced stability of the cation radical pair of [HMB$^{\bullet+}$,NO] relative to [XYL$^{\bullet+}$,NO] parallels the relative stabilities of the ground state complexes [HMB,NO$^+$] and [XYL,NO$^+$] as shown in Figure 10. Since the reverse order of stabilities is expected from Mulliken theory,[13] we conclude that the cation radical pair is not a suitable quantitative model for the charge-transfer excited states. The same conclusion is reached by the observation that identical spectral decays and quantum yields are observed from 355- and 532-nm excitation of the CT bands A and B in Table III.

(100) The earliest manifestation of complexation is expected to be the charge-transfer band—which may be fleeting in the light of the rapid (electron-transfer) followup process.

(101) The effects of complexation are most likely to be observed when the driving force for electron transfer is significantly less than complex formation (i.e. $RT \ln K_A$), as shown by the comparative behavior of HMB$^{\bullet+}$ and TOL$^{\bullet+}$ (see Table VIII and Figure 11), for which the electron transfer is (near) isoergonic and exergonic, respectively, in acetonitrile.

rodt), toluene, *tert*-butylbenzene (Eastman), chlorobenzene, iodobenzene, biphenyl (Matheson, Coleman, and Bell), ethylbenzene, isopropylbenzene, *o*-, *m*-, and *p*-xylene, 1,2,4-trimethylbenzene, durene, pentamethylbenzene (Aldrich), hexamethylbenzene (Kodak), mesitylene (Baker), naphthalene (Allied Chemical). 1,2-, 1,3-, and 1,4-dineopentyltetramethylbenzenes were gifts from M. S. Newman. Benzophenone (Baker) was purified by recrystallization from methanol. Hematoporphyrin IX (Aldrich) was purified by recrystallization from a mixture of acetone and chloroform to yield purple crystals which were dried in vacuo. Nitrosonium hexafluorophosphate, $NOPF_6$ (Pfaltz & Bauer), was used as received. Nitrosonium tetrafluoroborate, $NOBF_4$, was recrystallized by cooling a saturated acetonitrile solution of the salt to −20 °C under an atmosphere of argon for 12 h. The supernatant was then separated from the colorless crystals by filtration on a ground-glass Schlenk frit and dried in vacuo to yield colorless, free-flowing crystals. The nitrosonium salts were transferred, stored, and then weighed in a Vacuum Atmosphere HE-493 drybox kept scrupulously free of oxygen, water, and solvent vapors. Nitric oxide (Matheson) was purified by passing it successively through a 50% aqueous potassium hydroxide solution, concentrated sulfuric acid, and a cold trap maintained at −78 °C.

Solvent Purification. Dichloromethane (J. T. Baker) was repeatedly stirred with a quarter of its volume of concentrated H_2SO_4. The acid was changed twice daily, and stirring was continued for a week until the lower (acid) layer remained colorless. The upper layer was separated, washed twice with 5% aqueous sodium bicarbonate, washed with distilled water, and then dried over anhydrous calcium chloride. Finally it was distilled from P_2O_5 under an atmosphere of argon; the initial 10% of the distillate was rejected. Acetonitrile (HPLC grade, Fisher) was stirred for 24 h with 0.1% by weight $KMnO_4$, heated to boiling, cooled, and filtered from the brown MnO_2 residue. The filtered acetonitrile was distilled from P_2O_5 (~2 g L^{-1}) and redistilled from CaH_2 under an atmosphere of argon. Nitromethane (Fisher) was placed in a 2-L round-bottom flask that was protected by a drying tube containing $CaCl_2$ and cooled by immersion in a dry ice–acetone bath. The solvent was left undisturbed for 8 h until it was almost complete frozen. The slightly yellow liquid phase was carefully removed with the aid of a pipet and the frozen CH_3NO_2 was allowed to thaw. The freezing and thawing process was repeated twice and the resulting purified nitromethane was dried with anhydrous $CaCl_2$. The dried solvent was distilled at reduced pressure (bp 49–50 °C at 150 mmHg) in the dark from molecular sieves (Linde 4A activated at 300 °C for 8 h). All solvents were stored in the dark in Pyrex flasks (equipped with a Teflon needle valve and a viton O-ring) under an atmosphere of argon.

Instrumentation. UV–vis absorption spectra were measured on a Hewlett-Packard 8450A diode-array spectrometer. The time-resolved differential absorption spectra on the picosecond time scale were obtained with a laser-flash system that utilized the 532-nm (second harmonic) and 355-nm (third harmonic) 20-ps pulses from a Quantel YG501-C mode-locked Nd:YAG laser as the excitation sources. The excitation beam was focussed onto the sample with a cylindrical (fused silica) lens (*f* 2). The analyzing beam was produced by focussing the residual fundamental (1064 nm) on a mixture (1:1 (v/v)) of H_2O and D_2O contained in a 10-cm cuvette. The white light produced (400–800 nm) was focussed onto a bifurcated fiber bundle (Dolan Jenner) which directed the two analyzing beams through the excited and unexcited volumes of the sample at a 90° angle to the excitation beam. The analyzing beams passed through the sample and were collected by a fiber optic cable that was connected to a monochromator (ISA HR320). The signal was recorded on a dual diode array (Princeton Instruments DD512) that was calibrated with the 436- and 542-nm lines from a mercury lamp. Time resolution was achieved by passing the fundamental (1064 nm) along a delay stage (Velmex B4036Q13) to vary the path length of the probe light with respect to the excitation beam.

Samples were made up in a 1-cm precision quartz fluorimetry cell fitted with a Teflon stopcock. Concentrations of arene and $NO^+BF_4^-$ were adjusted so that the absorbance at the excitation wavelength was between 1.0 and 1.5. Before each spectral acquisition, a background data set was collected without exciting the sample. Absorbances were calculated from the following relation: $\Delta A = \log [(I_0 - I_0^b)/(I - I^b)]$, where I_0 represents the intensity of the analyzing beam passing through the unexcited volume of the cell, and I_0^b and I^b represent the background spectra, respectively. All spectra were acquired using an excitation energy of 2 mJ per laser pulse, and they represented the average of 300 transients.

The time-resolved spectral studies on the nanosecond/microsecond time scales were carried out with a spectrometer consisting of a Quantel YG580-10 Q-switched Nd:YAG laser with a pulse width of 10 ns. The second (532 nm) and third (355 nm) harmonics were used for excitation. The excitation energy was attenuated with various copper-wire mesh filters that were placed in the beam path. The probe beam consisted of the output from a 150-W Xenon arc lamp mounted in an Oriel housing that was equipped with an Aspherlab UV-grade condensing lens. The probe beam was focussed onto the sample, and the emerging beam from the sample was focussed onto the entrance slit of an Oriel 77250 monochromator. Depending on the spectral region studied, the following gratings were used: Oriel 77299, 1-μm blaze, 600 lines per mm for the 600–1050-nm region and Oriel 77298, 500-nm blaze, 1200 lines per mm for the 300–1000-nm region. The detector housing was attached to the exit slit of the monochromator. Either a Hamamatsu R928 photomultiplier tube (for the 200–800-nm region) or a Hamamatsu R406 photomultiplier tube (for the 600–1050-nm region) was used as the detector. A Kinetic Instruments lamp pulser was used to trigger the Xenon lamp to produce sufficient light intensity in the near-IR region. The timing sequence of the excitation and the probing of the sample were controlled by a Kinetic Instruments sequence-generator and laser-controller. Data acquisition and digitization were performed with a Tektronix 7104 oscilloscope in conjunction with a Tektronix C101 video camera and Tektronix DC501 software.

Measurement of the Quantum Efficiency of Cation Radical Formation: Nanosecond Time Scale. The quantum efficiencies for the formation of the arene cation radical upon excitation of the EDA complexes were measured by the method of relative actinometry.[58] For excitation at 355 nm, a solution of benzophenone in air-free benzene was used as the actinometer. The transient triplet of benzophenone with λ_{max} = 530 nm and ϵ_T = 7220 M^{-1} cm^{-1} (quantum yield for triplet formation ϕ_t = 1.0)[59] was monitored. Laser intensity was adjusted to 13 mJ per shot[102] at 355 nm. At this excitation energy, a plot of transient absorbance at 530 nm versus the ground-state absorbance at 355 nm was linear, with a zero intercept over a ground-state absorbance range of 0.0–0.6. Solutions of the aromatic donor and $NOBF_4$ [~1 mM $NOBF_4$ and ~3 mM arene for the 532-nm excitation and ~0.5 mM $NOBF_4$ and ~1 mM arene for the 355-nm excitation] were made up with ground-state absorbances in this range, and the transient absorbance was monitored at the λ_{max} of the cation radical (Table II). The time scale for observation (50–100 ns) was chosen so that negligible decay (<10%) of the signal was observed. Absorbances were recorded at three ground-state concentrations. Quantum yields were calculated using the following relationship: $\phi_{Ar^{+}} = (A_{Ar^{+}}/A_{BP})(7220/\epsilon_{Ar^{+}})$ where $A_{Ar^{+}}$ and A_{BP} are the absorbances of the cation radical and of triplet benzophenone, respectively, from solutions having the same ground-state absorbance at 355 nm. For the 532-nm excitation, a solution of hematoporphyrin IX (HP) in a mixture of MeOH and H_2O (9:1 (v/v)) buffered at pH = 7.3 was used as the actinometer.[60] The absorbance due to the triplet at 460 nm ($\Delta\epsilon$ = 10400 M^{-1} cm^{-1}, ϕ_T = 0.83) was monitored. The argon-purged actinometer solutions of HP showed transient absorptions at 460 nm that gave linear plots (with zero intercept) when plotted against ground-state absorbance at 532 nm (ground-state absorbance range 0.0–0.7; laser energy 12 mJ per shot). Transient absorbances of $Ar^{\bullet+}$ were determined between 50 and 100 ns, during which there was negligible absorbance change and all bimodal components had decayed. Quantum yields were calculated from the following expression: $\phi_{Ar^{+}} = 0.83(A_{Ar^{+}}/A_{HP})(10400/\epsilon_{Ar^{+}})$, where A_{HP} represents the transient absorbance of the HP solution (matched with the sample for ground-state absorbance) at 460 nm.[105]

Steady-State Irradiation of the Aromatic EDA Complexes with Nitrosonium. Acetonitrile solutions (3 mL) of HMB, PMB, and DUR (~3 mM) and $NO^+BF_4^-$ (~1 mM) were irradiated in a 1-cm cuvette equipped with a Teflon stopcock after the careful exclusion of air and moisture (vide infra). The irradiation was effected with a 1 kW Hg/Xe lamp (Hanovia XBO) equipped with a Pyrex filter to exclude light of λ < 320 nm. The UV–vis spectra of the solutions were monitored periodically to confirm the absence of spectroscopic changes of the CT bands. After the irradiation was carried out from 3 to 6 h, the red-brown solutions were quenched with water (10 mL). Extraction with dichloromethane yielded a colorless solution which upon quantitative gas chromatographic analysis by the internal standard method indicated the complete recovery of the aromatic donor.

Preparation of Samples for Spectroscopic Measurements and Picosecond Kinetics. The glassware used to prepare the solutions was stored at 150 °C in a oven overnight, assembled hot, and allowed to cool while

(102) To maintain the photon flux densities at $<10^{-8}$ einsteins cm^{-2}, as recommended by: Bensasson, R.; Goldschmidt, C. R.; Land, E. J.; Truscott, T. G. *Photochem. Photobiol.* **1978**, *28*, 277.

(103) (a) Oldham, K. B. *J. Electroanal. Chem.* **1981**, *122*, 1. (b) Aoki, K.; Osteryoung, J. *J. Electroanal. Chem.* **1981**, *122*, 19.

(104) Shoup, D.; Szabo, A. *J. Electroanal. Chem.* **1982**, *140*, 237. See Aoki and Osteryoung in ref 103b.

(105) The extinction coefficients for $Ar^{\bullet+}$ taken from Sehested et al.[45] were checked by an independent procedure based on charge-transfer photolysis of EDA complexes and found to be the same within experimental error. For the details, see supplementary material, Part II.

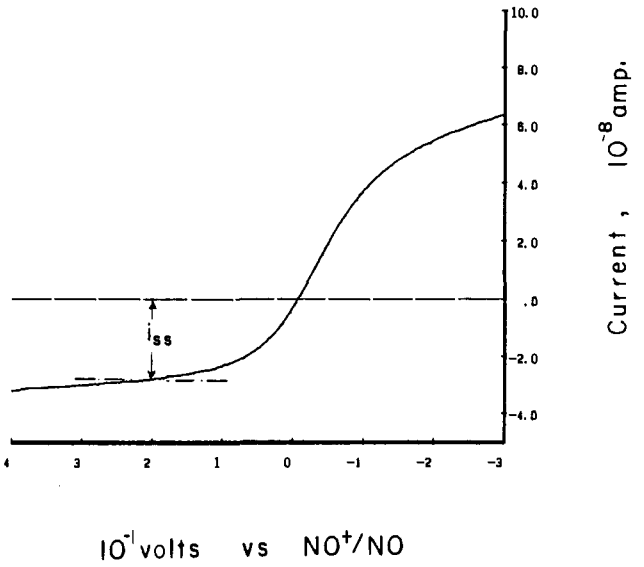

Figure 14. Slow scan voltammogram (v = 0.05 V s^{-1}) of an acetonitrile solution of 2.5 × 10^{-2} M $NO^+BF_4^-$ and 2.0 × 10^{-2} M HMB containing 2 mM NO. The curved line represents the cathodic ($i > 0$) and anodic ($i < 0$) current at the Pt microelectrode corresponding to the reduction of NO^+ and the oxidation of NO. The steady-state current, i_{SS}, was used to calculate the values of [NO] listed in Tables IV and V as described in the Experimental Section.

being evacuated on the vacuum line. A 50-mL volumetric flask equipped with a Teflon stopcock was introduced into the glovebox. Nitrosonium fluoroborate was also weighed and transferred to the flask in the glovebox. The arene was introduced into the flask against a strong counterflow of argon, and the flask was evacuated and refilled with argon. Solvent was transferred via cannula into a 50-mL Schlenk flask which contained activated alumina (predried for 12 h at 350 °C in vacuo). The solvent was allowed to stand for 5 min with occasional agitation and transferred using a Teflon cannula into the volumetric flask. The red-brown stock solution of the EDA complex was transferred with the aid of an all-glass syringe equipped with a Teflon needle to a quartz fluorimeter cell (Spectrocell, UV grade) equipped with a Teflon needle valve that had been previously evacuated and filled with argon. The fluorimeter cell was used as the sample for the spectroscopic as well as the picosecond kinetic experiments.

Cell for the Simultaneous Determination of NO Concentrations and Measurement of the Nanosecond Kinetics. The cell for these experiments consisted of separate chambers for the laser irradiation and the electrochemical measurements. The laser irradiation vessel consisted of 3-cm-long square quartz tubing (2 cm × 2 cm) connected via a graded quartz-to-Pyrex seal to a Kontes high-vacuum Teflon stopcock. The overall height of this chamber was 15 cm. This chamber was connected via a short (3 cm) length of Pyrex tubing (1-cm diameter) to the electrochemical cell which was topped with a Kontes screw-threaded joint for introduction of the microelectrode. A platinum wire, fused into the cell wall at a point close to the threaded joint, extended to the bottom of the cell and served as a quasireference electrode. The overall height, from cell bottom to threaded joint, of this chamber was 6 cm. The solution after its introduction into the cell was thus exposed only to glass, Teflon, and platinum. The cell was prepared for use by heating to 150 °C overnight, evacuating, and refilling with argon. The cell was charged with the stock solution of the aromatic donor and $NOBF_4$ (vide supra for preparation) as follows: the screw-threaded joint was removed and the cell closed with a septum. The stock solution was transferred to the electrochemical compartment using an all-glass syringe and a Teflon needle and the working electrode (vide infra) was introduced into the electrochemical compartment. During these operations, a continuous purge of the cell with argon was maintained. Electrochemical measurements were performed by tipping the cell so that the solution of the EDA complex flowed into the electrochemical compartment through the connector. The working electrode consisted of a platinum wire (Goodfellows, 25-μm diameter) fused into a glass rod, and the platinum wire fused on the cell (with area ~1 cm^2) served as a quasireference electrode.

Electrochemical Determination of Nitric Oxide Concentration. All voltammetric experiments were performed with a BAS 100B electrochemical analyzer using the platinum microelectrode. The voltammetry for the determination of the NO concentrations was performed in the cell described above using a Pt wire as quasireference electrode. Since NO^+ and NO were simultaneously present in solution, the potential at this quasireference was close to the formal potential of the NO^+/NO couple E_{NO^+} = +0.87, 0.98, and 1.00 V vs the ferrocene standard in CH_3CN, CH_3NO_2, and CH_2Cl_2, respectively. The potential at the microelectrode was swept very slowly ($v < 0.05$ V s^{-1}) positive, giving rise to the voltammetric plot similar to that shown in Figure 14. The anodic current due to NO oxidation reached a steady-state value and no further change in this current occurred upon further positive potential increases. The value of the limiting anodic current (subtracted from the zero-current baseline) is given by the following:[103] $i_{ss} = 4\mathcal{F}D_{NO}[NO]r$, where D_{NO} is the diffusion coefficient and r is the measured radius of the electrode. Thus the concentration is given directly by the steady-state current, i_{ss}, provided D_{NO} and r can be determined (vide infra). Owing to the small currents generated at the microelectrode (e.g., i_{ss} ~ 10 nA for [NO] = 0.2 mM), no supporting electrolyte was needed to enhance the conductivity of the solution. The values of D_{NO} and r for the determination of NO concentration were determined chronoamperometrically. A solution of ferrocene (f) dissolved in the solvent of interest containing 0.01 M (CH_3CN and CH_3NO_2) or 0.1 M (CH_2Cl_2) $TBAPF_6$ was introduced into a three-electrode cell using a hypodermic syringe. The working electrode was the Pt microelectrode used in the NO determinations, and the auxiliary electrode consisted of a Pt grid. A saturated calomel electrode served as the reference. The potential at the working electrode was pulsed (rise time ~10 μs) and the current at the working electrode was measured and stored on the BAS analyzer for times between 2 and 200 ms. After 20 s, the value of the limiting current was determined. The time-dependent transient current is given by the following:[104] $i/i_{ss} = 1/2\pi^{1/2}P^{-1/2} + \pi/4 + 0.095P^{1/2}$ ($P < 1.44$) and $i/i_{ss} = 1 + 0.7184P^{-1/2} + 0.0562P^{-3/2}$ ($P > 0.88$), where $P = 4D_f t r^{-2}$, i_{ss} is the limiting current from this experiment, D_f is the diffusion coefficient of ferrocene, and r is the radius of the electrode. The experimental (i vs t) curve was simulated using the ratio $D_f r^{-2}$ as the sole adjustable parameter. The two factors can be separated, since the steady-state limiting current is also determined, and $rD_f = i_{ss}/4\mathcal{F}C_f$, where C_f is the concentration of ferrocene. The values of D_{NO} were determined by chronoamperometry in the solvent of interest. Solutions of NO were prepared by briefly introducing NO into the head space of a 3-electrode cell while stirring the solvent/electrolyte mixture. When the potential at the Pt microelectrode was pulsed to +1.5 V for CH_3CN vs SCE, or +1.6 V for CH_3NO_2 and CH_2Cl_2, it produced the time-dependent transient currents which were recorded and stored. The experimental current vs time function was simulated as before, using the equation above for i/i_{ss}. The value for $D_{NO}r^{-2}$ was determined by this simulation, and the value of D_{NO} was calculated from r determined with ferrocene (see Table X). The decreasing value of r_{NO} [in the order $CH_3CN > CH_2Cl_2 > CH_3NO_2$] contrasts with the relative invariance of the Stokes–Einstein radius of ferrocene, and it points to a profound change in the solvation of NO. Indeed the diffusional radius of NO is the largest in the strongly donating solvent CH_3CN, which is indicative of its stronger interaction with CH_3CN compared to either CH_3NO_2 or CH_2Cl_2. The order of solvation parallels the more profound changes induced by the solvation of NO^+ cation.[14]

Table X. Measurement of Diffusion Constants of Nitric Oxide by Microvoltammetry

solvent	D_f[a] (10^5 cm^2 s^{-1})	D_{NO}[a] (10^5 cm^2 s^{-1})	r_f[b] (Å)	r_{NO}[b] (Å)
CH_3CN (14.1)[c]	1.9	1.6	3.3	4.0
CH_3NO_2 (2.7)[c]	1.1	3.2	3.3	1.1
CH_2Cl_2 (0)[c]	1.4	2.2	3.7	2.4

[a] Diffusion coefficients of ferrocene (D_f) and nitric oxide (D_{NO}), evaluated for 2–3 mM solutions using a Pt microelectrode (r = 12.5 μm) by chronoamperometry at 25 °C. [b] Stokes–Einstein radius of ferrocene (r_f) and NO (r_{NO}), calculated as $r_x = k_B T/6\pi\eta D_x$ where η is the viscosity of the solvent at 25 °C and k_B is Boltzmann's constant. [c] Gutmann donor number in parentheses.

Acquisition of the NO-Dependent Nanosecond–Microsecond Decays. Immediately upon the determination of the NO concentrations, the solution was tipped through the transfer arm of the cell into the spectrochemical compartment for the spectroscopic studies. The cell was then removed from the photolysis apparatus and attached, via the Teflon needle valve, to a dual gas (NO and argon) line. After thorough purging of the cell and the gas line with argon, NO was introduced into the head space of the spectroelectrochemical apparatus. The introduction of NO for 2–3 min resulted in an increase of the NO concentration (0.1–0.2 mM), present adventitiously in the stock solution to 7–15 mM. The cell was then closed and removed from the gas manifold, and the concentration of NO was determined by voltammetry. After acquisition of the fast kinetics data, the concentration of NO was reduced by flushing the

head space of the cell with argon and stirring the solution for ~10 min. Electrochemical and fast kinetics experiments were repeated on the solution and the NO was further reduced by flushing. Generally, 5 to 6 different NO concentrations could be achieved before the concentration returned to 0.1–0.2 mM. Laser intensities for the kinetic measurements were generally 15 mJ per shot, except when a variable intensity was desired. A series of 10 to 20 transients was averaged and 3 to 5 data sets were examined in order to ensure reproducibility. Decays were fitted to first-order, second-order, or mixed first- and second-order decays using ASYST 2.0 software operating on an AT&T 6300-plus microcomputer.

Decay Kinetics of the Aromatic Cation Radicals. The picosecond absorbances at λ_{max} for the cation radical (490, 480, 460, and 440 nm for $HMB^{\bullet+}$, $PMB^{\bullet+}$, $DUR^{\bullet+}$, and $XYL^{\bullet+}$) were normalized and plotted as a function of time using the HYPERPLOT program. A decay curve was simulated according to the following expression: $A_t/A_0 = (1 - \phi)\cdot \exp[-(k_1 + k_s)t] + \phi$ using both the sum $(k_1 + k_s)$ and ϕ as adjustable parameters. Successive decay curves, generated by changing the value of $(k_1 + k_2)$ or ϕ, were superimposed on the experimental points until the fit was acceptable.[106] For $TOL^{\bullet+}$, no positive absorbance in the region 400–600 nm was observed on the picosecond time scale. Kinetics of this species were obtained by measuring the return of the negative absorbance (due to the bleaching of the CT band, monitored at λ = 430 nm) to a zero baseline absorbance. The time constant for this process ($\sim 10^{10}$ s^{-1}) was taken as $(k_1 + k_s)$ and the separation of k_1 and k_s was achieved by assuming that the k_s for $TOL^{\bullet+}$ and NO is the same as that for $XYL^{\bullet+}$ and NO. Thus an estimated value of $k_1 \sim 2 \times 10^{10}$ s^{-1} was obtained for the back-electron transfer from the $[TOL^{\bullet+},NO^{\bullet}]$ complex.

The observed ns/μs time-dependent absorbance at λ_{max} for the arenes was fitted to first-order, mixed first- and second-order, or second-order decays using the ASYST (2.0) software. Only the first set of decays were used in the determination of k_{11} (and k_a). The plot of k_{obs} vs [NO] showed distinct curvature (especially for HMB and PMB), so that the limiting value of $k_{obs}/[NO]$, taken at [NO] < 0.5 mm, was equated to k_{11}. The exact expression for the slow component of the biphasic decay predicted for Scheme III is given by the following: $k_{obs} = 1/2\{k_1 + k_s + k_a[NO] - [(k_1 + k_s + k_a[NO])^2 - 4k_1k_a[NO]]^{1/2}\}$ (see Appendix for the derivations of this expression.) To obtain k_a, k_{obs} was plotted against [NO] and trial values of k_a were used to generate the plots of k_{obs} versus [NO], which were superimposed on the experimental points. The simulated k_{obs} was generated from the equation above and the values of k_1 and k_s determined from the picosecond kinetic experiments. Adjustment of k_a was carried out until the experimental points fitted the simulated (practically linear) curve to an acceptable degree, as judged by visual inspection of the plots. The adjusted values of k_a are those reported in Table VIII. The values of k_{obs} obtained from the simulation also yielded the second-order constant $k'_2 = k_{obs}[NO]^{-1}$. Since k'_2 always agreed (±10%) with k_2^{IS} obtained from the steady-state expression (eq 25), it is listed in Table VIII as k_2^{IS}.

Acknowledgment. We thank S. J. Atherton and P. T. Snowden (Center for Fast Kinetics Research) for helpful advice, the National Science Foundation, the R. A. Welch Foundation, and the Texas Advanced Research Program for financial support, and the University of Warsaw for the leave of absence for Z.J.K.

(106) The further refinement of the picosecond decay kinetics with the aid of two least-squares curve fitting procedures yielded values of k_1 and k_s that did not differ significantly from the values listed in Table VII. For details see the supplementary material, Part I.

Appendix: Derivation of the Exact Solution for Electron Transfer Combined with Association/Dissociation

For Scheme III, let x be the concentration of $Ar^{\bullet+}$ in the EDA complex and y be the concentration of $Ar^{\bullet+}$ that is freely diffusing. The differential equations governing this system are as follows: $dx/dt = -ax + by$ and $dy/dt = cx - by$, where $a = (k_1 + k_s)$, $b = k_a[NO]$, and $c = k_s$. Substitution for y and dy/dt gives the second-order differential equation for $x(t)$

$$d^2x/dt^2 + (a + b)\, dx/dt + (ab - bc)x = 0$$

which has a solution $x(t) = C_1 \exp(-\lambda_1 t) + C_2 \exp(-\lambda_2 t)$, where $\lambda_1 = 1/2\{a + b + [(a + b)^2 - 4(ad - bc)]^{1/2}\}$ and $\lambda_2 = 1/2\{a + b - [(a + b)^2 - 4(ad - bc)]^{1/2}\}$ and $C_1 = (\lambda_2 + a)/(\lambda_2 - \lambda_1)$ and $C_2 = (a + \lambda_1)/(\lambda_2 - \lambda_1)$ are constants of integration. Similarly, the time dependence for the uncomplexed $Ar^{\bullet+}$ can be expressed as $y(t) = C_3 \exp(-\lambda_1 t) + C_4 \exp(-\lambda_2 t)$. Since $A_t = y(t) + x(t)$, the rate constant for the fast decay is given by λ_1 and that for the slow decay by λ_2, i.e.[107]

$$\lambda_1 = 1/2\{k_1 + k_s + k_a[NO] + [(k_1 + k_s + k_a[NO])^2 - 4k_1k_a[NO]]^{1/2}\} \quad (27)$$

and

$$\lambda_2 = 1/2\{k_1 + k_s + k_a[NO] - [(k_1 + k_s + k_a[NO])^2 - 4k_1k_a[NO]]^{1/2}\} \quad (19)$$

In the limit where $k_a[NO] \ll k_1$, the expression in eq 27 for the fast decay simplifies to

$$\lambda_1 = 1/2\{k_1 + k_s + k_a[NO] + [(k_1 + k_s + k_a[NO])^2]^{1/2}\} \simeq k_1 + k_s + k_a[NO] \simeq k_1 + k_s \quad (28)$$

which is given in eq 16 of the text. The slow decay can similarly be reexpressed in the simpler form as

$$\lambda_2 = k_1k_a[NO]/(k_1 + k_s + k_a[NO]) \quad (29)$$

by the series expansion of eq 19 followed by the truncation of the higher order terms with $4k_1k_a[NO]/(k_1 + k_s + k_a[NO])^2 \ll 1$ for [NO] < 0.1 M. When $(k_1 + k_s) \gg k_a[NO]$ as described in Tables VII and VIII, a further simplification yields the steady-state expression in eq 25.

Supplementary Material Available: Nonlinear least-squares fittings of the picosecond decays and extinction coefficients of transient polymethylbenzene cation radicals, including listings of two-parameter least-squares nonlinear fits for picosecond decays, comparison of two- and three-parameter nonlinear least-squares fitting of picosecond data, and extinction coefficients of methylbenzene cation radicals as well as transient absorption spectra of hexamethylbenzene and tetracyanobenzene anion radical (16 pages). Ordering information is given on any current masthead page.

(107) We thank T. Yabe for the mathematical solution of the kinetics in Scheme III.